Homodyne dynamic light scattering in supramolecular polymer solutions: anomalous oscillations in intensity correlation function

Emilie Moulin, Irina Nyrkova, Nicolas Giuseppone, Alexander Semenov, Eric Buhler

Homodyne Dynamic Light Scattering in Supramolecular Polymer Solutions: Anomalous Oscillations in Intensity Correlation Function

Emilie Moulin, [1,†] **Irina A.Nyrkova,** [1,†] **Nicolas Giuseppone,** [1] **Alexander N.Semenov,** [1,*] **Eric Buhler** [2,*]

[1] *Institut Charles Sadron (ICS), CNRS - UPR 22, Université de Strasbourg, 23 rue du Loess, BP 84047, 67034 Strasbourg Cedex 2, France*

[2] *Matière et Systèmes Complexes (MSC), UMR 7057, Université de Paris (Université Paris Diderot), Bâtiment Condorcet, 10 rue Alice Domon et Léonie Duquet, 75205 Paris Cedex 13, France*

(January 31, 2020)

† Contributed equally to this work

∗ Corresponding authors:
alexander.semenov@ics-cnrs.unistra.fr, eric.buhler@univ-paris-diderot.fr

Abstract

Dilute solutions of electronically active molecules capable of irradiation-driven supramolecular self-assembly are studied by dynamic light scattering. We detect unusual well-defined oscillations in the long time range of the homodyne intensity correlation function for all solutions that were irradiated with white light prior to the measurements. The oscillation effect is attributed to the local laser-induced heating of the samples due to strongly enhanced absorption manifested by the supramolecular filaments. It is found that the oscillation frequency depends on the irradiation time, solution concentration, and the incident laser power, but is independent of the scattering angle. These observations are explained with a semi-quantitative theory relating the oscillation effect to thermo-gravitational convection flows generated by laser beam. The results suggest that the presence of such homodyne oscillations could be a sensitive probe for aggregation in many complex systems.

1. Introduction

Light scattering has provided an important tool to characterize the structure, local dynamics and motions of particles in complex systems [1]. Indeed, polymer solutions and gels, supramolecular self-assemblies and colloidal dispersions have been routinely studied with laser light scattering for many decades [1–5].

Dynamic light scattering (DLS) in particular turned out to be a powerful technique allowing to discriminate between solute particles of different sizes and to determine the particle size distribution in a solution or suspension [1,3,4,6–9]. This method permits investigation of mixtures of widely disparate species whose relaxation times may differ by many orders of magnitude.

A topical example for DLS application concerns self-assembly processes in solutions of molecular building blocks connected by noncovalent reversible associations (leading to formation of associative polymers, gels, fibrils, micelles, vesicles, and other supramolecular materials) [1,2]. Such systems typically involve mesoscopic or macroscopic structures whose composition can vary in response to external stimuli (temperature, pH, concentration, light). [10–13] The DLS signal is determined through dynamical correlations of local electric polarizations in the system, and their relaxation reflects the kinetics of the composition changes. In particular, DLS proved to be a very efficient tool to study self-assembly processes initiated by external triggers [6–9,12–14].

However, the DLS studies of the evolution in the self-assembling systems are not always straightforward, as such systems are typically characterized by multiple length-scales and time-dependent nature of responsive polydisperse assemblies. Moreover, the associating units themselves can cause light absorption, fluorescence, plasmonic and other effects compromising the standard DLS protocol. To overcome these problems in studying novel highly complex self-assembling systems, it is essential to develop new experimental strategies characterizing the dynamics (including local velocities and mobilities) of all individual species involved in the system.

A key difficulty met in many supramolecular and macromolecular systems is related to the *light absorption* causing such unwanted side effects as local heating, convection and thermal diffusion. This often imposes restriction on the concentration range accessible to the experiments. The complications arising from light absorption have deterred researchers from studying many complex systems using light scattering. The main consequences of local heating due to absorption are the appearance of the so-called thermal lens (which causes the incident laser beam to diverge) and the anomalous oscillations arising in the intensity-intensity correlation function measured by the homodyne DLS [15–17].

In this paper, we study such unusual long-lasting *regular oscillations* in homodyne DLS spectra observed in scattering of multicomponent supramolecular dispersions based on self-assembling triarylamines (TAA) forming highly conductive nano-wires upon irradiation [12,13,18–22]. We discuss the possible origins of these oscillations and respective specific details of their manifestation. We show that, despite complications due to light absorption, the oscillations in the low-frequency spectrum of the homodyne DLS can be used to characterize the system, in particular, to provide information on the drift velocities of the scattering particles in solution. Note that it is the heterodyne light scattering (laser doppler velocimetry where the incident beam is mixed with the scattered beam) that is typically used

to measure the drift velocity [23–29]. In this paper we demonstrate, however, that observation of oscillations with a *homodyne* DLS can provide a simple alternative to the more involved and complicated heterodyne DLS studies [1].

The paper is organized as follows. In the next section we describe the light-absorbing TAA systems and the DLS technique employed in the paper. Section 3 presents detailed DLS data on intensity correlations in TAA solutions involving unusual oscillations in their homodyne spectrum. We show that the oscillation frequency depends on the irradiation time, concentration, and the incident laser power, but is independent of the scattering angle. These observations are explained from a theoretical standpoint by relating the oscillation effect to thermo-gravitational convection flows generated by the laser beam. Section 4 is devoted to the related discussion and theoretical analysis of the obtained homodyne DLS results.

2. Materials and methods

2.1. Formation and properties of TAA nanowires

We conduct our detailed analysis on solutions of triarylamine (TAA) derivatives with tailored side-groups that are capable to self-assemble into highly conductive supramolecular nanowires upon white light exposure [12–14,30]. The nature of multi-stage cooperative self-organization of TAA entities was elucidated in detail by a combination of experimental and theoretical tools in our previous works [14,30]. Some key features are illustrated in Fig. 1 for a typical example of monoamine triaryl molecule (triarylamine). In the present experiments we exploited the same TAA molecules whose systems have been well-characterized for all stages of their self-assembly process in chloroform [14]. In particular, we showed that the light-induced aggregation is initiated by radical cations $TAA^{\cdot}+$ which are formed by photon-excitation of the TAA unimers in an oxidating solvent (stage (i) in Fig. 1a). The radicals (adopting the form of $TAA^{\cdot}$+Cl- dipoles) first aggregate with themselves (via dipole-dipole attraction) and then with neutral TAA forming the double-columnal critical nucleus by charge transfer in conjunction with hydrogen bonding (of amide groups) and $\pi - \pi$ stacking of aryl rings (stage (ii)). The short fibril fragments then grow in length via end attachment of free TAA molecules (stage (iii)). Finally, the fibrils aggregate both end-to-end and laterally forming micrometer-long and few-nanometer thick stable bundles serving as nanowires (stage (iv)). These nanowires, if formed under irradiation, were proved to show high metallic electric conductivity; they can induce plasmonic effects and give the solution a specific bright dark green color (whereas the original unimeric TAA solution has a light yellow color).

It is important to stress that the original unimeric TAA chloroform solutions are stable in the dark for months. Apart from white-light initiation, the self-assembly process can be provoked also by adding a small amount of an oxidant, or by adding of the so-called 'seeds' (small ultra-sonicated fragments of fibrillated TAA). For short light-pulses the self-assembly could take a significant time (up to an hour for 1s-pulses), but it takes just a few seconds for the light exposure of 5s. Our analysis [14] showed that initial purely unimeric solutions can self-assemble only in the presence of radicals, and that the critical nucleus for the TAA assembly consists of ~ 6 monomers including ≥ 3 radicals. As a result, nucleation rate must

strongly depend on concentration, hence the nucleation essentially stops soon after the beginning of the fibril formation, well before the reservoir of TAA is depleted, so that the thinnest fibrils (with no lateral aggregation) may be expected have roughly the same length at the end of the self-assembly process [14]. However, the solute is typically dominated with 'wires' of different thickness (double fibrils and their lateral stacks, bundles) which, considered together, show a significant length polydispersity because the effective growth rate depends on the bundle thickness (and due to rare structural defects preventing further elongation of an aggregate).

Onces formed, the TAA fibrils are extremely stable, their local structure was proved to be unchanged for many months of incubation in the dark (a slow growth of fibril length was nevertheless observed due to concatenation of fibrils). Besides, the fraction of the radicals in fibrils f (originally in the range of $f \simeq 10 - 20\%$ after a 1-hour irradiation) slowly decreases during the dark incubation (within a time-scale of 1-2 hours f approaches $\sim 5\%$ and then decays as $f \propto 1/t$), but it can be recovered after an extra stage of white-light illumination. The qualitative behavior of the radical amount is reflected in the UV-vis absorption spectra, Fig. 1d. While the freshly-formed TAA fibrils with $f > 10\%$ are highly conductive and brightly green upon the irradiation, the same fibrils with $f < 3\%$ are brownish and less conductive. The fibrils which were initiated by seeding or a short white-light pulse are almost colorless or slightly yellow, similar to the original unimeric TAA solution.

We established that both the radical loss and recovery take place at the fibril ends where the radicals can either be formed by photon absorption or decay via pairwise radical annihilation. The pairwise nature of the radical decay (which demands the simultaneous presence of two radicals at a fibril end) together with the slow character of radical diffusion (from the middle of a fibril to its ends) ensures the apparent persistence of the radicals (their decay as $f \propto 1/t$ is much slower than the ordinary exponential law).

2.2. Experimental specifications

The details of TAA synthesis, purification, chloroform solution preparation and irradiation are described in refs. [12–14]. White visible light irradiation was done with a 20W glow-filament lamp located at 5 cm from the sample (a glass test tube with TAA solution). Absorption spectra (Fig. 1d) were recorded using a UV-Vis-NIR spectrophotometer Cary 500 scan Varian in quartz glass cuvette with 1.0 cm optical path.

The homodyne dynamic light scattering (DLS) measurements were performed in UMR-7057 laboratory using a 3D DLS spectrometer (LS Instruments, Fribourg, Switzerland) equipped with a 25mW HeNe laser (JDS uniphase) operating at λ_0 =632.8nm (beam diameter 0.7mm at $1/e^2$ of maximum intensity, beam divergence 1.15 mrad), a two-channel multiple tau-correlator (1088 channels in autocorrelation), a variable-angle detection system, and a temperature-controlled index matching vat (LS Instruments); the temperature was fixed to $T = 293$K. The scattering spectrum was measured using two single mode fiber detectors and two high sensitivity APD detectors (Perkin Elmer, model SPCM-AQR-13-FC). The power of the incident and transmitted laser beams was measured using a Thorlabs PM 100 high sensitivity optical power meter.

The principal optical scheme of the DLS setup is shown in Fig. 2. The incident laser beam (of diameter $d_{beam} \approx 2$mm at L1) is focused on the sample with the lens L1 (focal length $F_1 = 250$mm), so that the illuminated volume has cross-section diameter of $d_{sc} \sim 100\mu$m [5]. The beam cone divergence angle in the sample is

$$\Delta\theta_{sc} \approx d_{beam}/F_1 \approx 8 \cdot 10^{-3} \tag{1}$$

The scattering light is collected with the lenses L2 ($F_2 = 250$mm) and L3 ($F_3 = 3.9$mm) onto an optical fiber (with the optical core diameter $d_4 = 4\mu$m) connected to an efficient avalanche photodiode detector (APD). The lens L2 is placed at distance $x_2 = F_2$ from the sample. The scattering volume accessible for the detector is nearly cylindrical with the diameter d_{sc} and the length L_{sc} along the primary laser beam,

$$L_{sc} \approx F_2 d_4/F_3 \approx 260\mu m \tag{2}$$

For the DLS studies, dilute solutions of monomeric TAA were prepared in deuterated chloroform $CDCl_3$ and transferred into 5 mm diameter cylindrical scattering cells. Dust and impurities were removed from the samples before irradiation by filtration through 0.22μm PTFE Millipore filters. Prior to irradiation with visible light, no evidence for the presence of self-assemblies or larger objects could be deduced from the DLS: no characteristic decays were observed in the intensity correlation function apart from the unimer mode with relaxation time $\tau_{uni} \simeq 3\mu$s corresponding to the average geometrical size of $\sim$1nm (cf. Figs. 1b,c). Moreover, no aggregates were detected after a long (up to 8 hours) DLS run at a maximum laser intensity ($P_0 = 22$mW), proving that irradiation at wave-length λ_0 =632.8nm does not induce any TAA self-assembly.

Figure 1d shows the UV-Vis spectra of a 1 mM solution of TAA in chloroform in the absence of light irradiation (0s), for samples irradiated for some time (765s, 3765s), and for a solution first irradiated during $t = 3765$s and then stored in the dark for 14400s (4h). We observe that the irradiated supramolecular solutions do absorb light; in particular, the absorbance around 633 nm (the laser wavelength used in our light scattering experiments) strongly increases with the irradiation time, saturating for $t > 3000$s. By comparison, incubation of irradiated solutions in the dark leads to a decrease of the absorbance. Thus, light absorbance of TAA solutions strongly depends on their aggregation state and irradiation pre-history.

2.3. Homodyne and Heterodyne Dynamic Light Scattering (DLS) techniques

The setup of Fig. 2 implies irradiation of the sample with a V-polarized laser light. The scattering vector is

$$\underline{q} \equiv \underline{k}_2 - \underline{k}_1; \qquad q = \frac{4\pi n}{\lambda_0} \sin\left(\frac{\theta}{2}\right) \tag{3}$$

where $\underline{k}_1$ and $\underline{k}_2$ are wave-vectors of the incident and scattered light (which are both parallel to a horizontal plane), n is refractive index of the sample ($n = 1.445$ at $T = 20^0$C for pure $CDCl_3$), and θ is the scattering angle.

Here it is taken into account that the scattering from particles moving with thermal speeds (v_T) is typically quasi-elastic (as $v_T \lesssim 100\text{m/s} \ll c_l = 3 \times 10^8\text{m/s}$, the velocity of light), hence $k_2 = k_1 = k = 2\pi n/\lambda_0$.

The scattered electric field $E_{true}(t) = \Re\left[E\exp(i\omega t)\right]$ [1] at the detector is determined by the actual positions of the scattering centers $\underline{r}_m(t)$ present in the scattering volume V:

$$E \propto c_V(\underline{q},t) \equiv \sum_m{}' \exp\left(i\underline{q}\cdot\underline{r}_m(t)\right) \tag{4}$$

where $c_V(\underline{q},t)$ is the Fourier transform of the particle concentration $c_V(\underline{r},t)$ calculated over the scattering volume V (here and below the prime over summation means that it includes only those particles that are present in the scattering volume V at the given time t). Eq. (4) is valid in the quasi-elastic approximation, that is, if the scattering centers move slowly with speed $v_T \ll c_l\lambda/L_{sc}$, which is typically true for soft matter studies (here $L_{sc} \sim 0.1 - 1\text{mm}$ is the linear size of the scattering volume).

The instantaneous intensity of the scattered light is $I_{true}(t) = c_l E_{true}(t)^2/4\pi$, while the mean intensity (averaged over the oscillation period $2\pi/\omega$) is:

$$I(q,t) = \frac{c_l}{8\pi}\left|E\right|^2 = \frac{c_l}{8\pi}EE^* \propto \sum_m{}' \sum_n{}' \exp\left(i\underline{q}\cdot[\underline{r}_m(t) - \underline{r}_n(t)]\right) \tag{5}$$

When the mutual positions of the scattering particles $\underline{r}_m(t)$ change, the field E, eq. (4), and the intensity I, eq. (5), change accordingly. Hence, time correlations in the slow-changing (compared to the light frequency) $E(t)$ and $I(t)$ functions carry information about the particle motions.

The following two time-correlation functions are useful for interpretation of DLS experiments: the autocorrelation function of the field:

$$G^{(1)}(q,\tau) \equiv \left(\frac{c_l}{8\pi}\right)\langle E^*(q,0)E(q,\tau)\rangle \tag{6}$$

and of the intensity:

$$G^{(2)}(q,\tau) \equiv \langle I(q,0)I(q,\tau)\rangle \tag{7}$$

The statistical averages in eqs. (6), (7) are equivalent to time-averages over a long enough time, t_{DLS} :

$$\langle X(0)X(\tau)\rangle = \frac{1}{t_{DLS}}\int_0^{t_{DLS}} X(t)X(t+\tau)\mathrm{d}t \tag{8}$$

The function $G^{(2)}$, is often called the *homodyne* correlation function, is directly measured by the 2-channel tau-correlator connected to the photomultiplier light detectors of the DLS setup. Eqs. (4), (5), (7) connect $G^{(2)}$ with correlations of the scattering particles:

$$G^{(2)}(q,\tau) \propto F_2(\underline{q},\tau) \equiv \left\langle c_V(\underline{q},\tau)c_V^*(\underline{q},\tau)c_V(\underline{q},0)c_V^*(\underline{q},0)\right\rangle \tag{9}$$

---

[1] Here $\Re$ and $\Im$ mean the real and imaginary parts of a complex number.

In accordance with eq. (4) the function $G^{(1)}$ (called the *heterodyne* correlation function) is proportional to the dynamic structure factor (autocorrelation function of concentration fluctuations):

$$G^{(1)}(q,\tau) \propto F_1(\underline{q},\tau) \equiv \left\langle c_V(\underline{q},\tau) c_V^*(\underline{q},0) \right\rangle \tag{10}$$

It can be directly measured with the so-called *heterodyne* DLS, when a portion the incident laser beam (E_0) is *added* to the scattered light E, eq. (4), hence the resulting field at the detector will be $E_{true}(t) = \Re\left[(E_0 + E)\exp(i\omega t)\right]$, where E_0 includes the phase shift. The DLS-measured count-rate autocorrelation function is then

$$G^{(2)}_{het}(q,\tau) \equiv \langle I_{het}(q,\tau) I_{het}(q,0) \rangle \tag{11}$$

where $I_{het}(t) = (c_l/8\pi)\left|E_0 + E(t)\right|^2$, cf. eq. (5). With no fluctuations of the added light ($E_0(t) = E_0 = \text{const}$), we get

$$G^{(2)}_{het}(q,\tau) \simeq I_0^2 + 2I_0 G^{(1)}(q,0) + 2I_0 \Re\left[G^{(1)}(q,\tau)\right] + G^{(2)}(q,\tau) \tag{12}$$

where $I_0 = c_l \left|E_0\right|^2 / 8\pi$ is the added light intensity and the terms involving $E(0)E(\tau)$, or those linear or cubic in E are omitted as they vanish for $d_{sc} \gg 1/q$. If the added incident field E_0 dominates the scattered signal: $|E_0| \gg |E|$, the last quadratic term in eq. (12) can be neglected, hence

$$G^{(2)}_{het}(q,\tau) \simeq A + \Re\left[G^{(1)}(q,\tau)\right]/B$$

where A and B are constants (independent of τ). Therefore indeed the heterodyne DLS allows for determination of the real part of the heterodyne correlation function:

$$\Re\left[G^{(1)}(q,\tau)\right] = B\left(G^{(2)}_{het}(q,\tau) - G^{(2)}_{het}(q,\infty)\right) \tag{13}$$

since $G^{(1)}(q,\infty) = 0$ for a system in the liquid state.

In practice the DLS experiments are often described using the normalized heterodyne and homodyne correlation functions (cf. eqs. (6), (7)):

$$g^{(1)}(q,\tau) \equiv \frac{G^{(1)}(q,\tau)}{G^{(1)}(q,0)} = \frac{F_1(q,\tau)}{F_1(q,0)} \tag{14}$$

$$\Re\left[g^{(1)}(q,\tau)\right] = \frac{\left(G^{(2)}_{het}(q,\tau) - G^{(2)}_{het}(q,\infty)\right)}{\left(G^{(2)}_{het}(q,0) - G^{(2)}_{het}(q,\infty)\right)} \tag{15}$$

$$g^{(2)}(q,\tau) \equiv \frac{\langle I(q,\tau) I(q,0)\rangle}{\langle I(q,0)\rangle^2} = \frac{G^{(2)}(q,\tau)}{G^{(2)}(q,\infty)} = \frac{F_2(q,\tau)}{F_2(q,\infty)} \tag{16}$$

Hence, $g^{(1)}(q,0) = 1$ and $g^{(2)}(q,\infty) = 1$ by definition. Note that $G^{(1)}(q,0) = \frac{c_l}{8\pi}\left\langle |E(q)|^2 \right\rangle \equiv I(q)$ gives the angular dependence of the time-averaged scattering intensity (here $I(q) = \langle I(q,t)\rangle$, where $I(q,t)$ is defined in eq. (5)). Similarly, $G^{(2)}(q,\infty) = I(q)^2$, $G^{(2)}_{het}(q,\infty) = I_{het}(q)^2$ ($I_{het}(q)$ is defined in analogy with $I(q)$), so

$$g^{(2)}(q,\tau) \equiv \frac{\langle I(q,\tau) I(q,0)\rangle}{I(q)^2} \tag{17}$$

2.4. Interpretations of the DLS correlation functions in some simple cases

For illustration purposes we present below the relationships between the DLS correlation functions and the self-intermediate scattering function for some simple model systems.

Let us define the particle status function [1]

$$b_m(t) \equiv \begin{cases} 1, & \text{if } m \in V \\ 0, & \text{if } m \notin V \end{cases} \tag{18}$$

which shows if a particle m belongs to the scattering volume V at time t. Then

$$c_V(\underline{q}, t) = \sum_m b_m(t) \exp\left(i\underline{q} \cdot \underline{r}_m(t)\right), \tag{19}$$

$$c_V(0, t) = \sum_m b_m(t) = N(t) \tag{20}$$

where $N(t)$ is the current number of particles in V. The summations here are now performed over the whole system (cf. (4)). Next, we define the ***self-intermediate scattering function***

$$F_s(\underline{q}, \tau) \equiv \left\langle \exp\left(i\underline{q} \cdot [\underline{r}_m(\tau + t) - \underline{r}_m(t)]\right)\right\rangle \tag{21}$$

which characterizes the displacement of a particle during time τ. It is important to stress that we consider the ***stationary*** systems only in this study: any joint probability distribution does not change with a time shift t, so F_s depends on τ, but not on t. For $q \neq 0$

$$F_s(\underline{q}, 0) = 1 \qquad \text{and} \qquad F_s(\underline{q}, \infty) = 0 \tag{22}$$

2.4.a. Ideal case: dilute solution of identical point-like particles

If the scattering particles do not interact directly with each other (the solution is dilute enough), their trajectories are statistically independent. Hence,

$$F_1(\underline{q}, \tau) = \left\langle \sum_m b_m(\tau) b_m(0) \exp\left(i\underline{q} \cdot [\underline{r}_m(\tau) - \underline{r}_m(0)]\right)\right\rangle \tag{23}$$

cf. (10), (19) and note that in the light-scattering experiments the zero scattering wave-vector is always excluded: $q \neq 0$, hence $\left\langle \exp(i\underline{q} \cdot \underline{r})\right\rangle = 0$. We also note that the exponential factor in eq. (23) reflects the statistical properties of the particle displacement $\Delta\underline{r}_m(\tau) \equiv \underline{r}_m(\tau) - \underline{r}_m(0)$ which are expected to be the same for all particles in the scattering volume V. It is obvious that $b_m(\tau)b_m(0)$ and $\Delta\underline{r}_m(\tau)$ are statistically nearly independent if

$$|\Delta\underline{r}_m(\tau)| \ll L_{sc} \tag{24}$$

so

$$F_1(\underline{q},\tau) \simeq \sum_m \langle b_m(\tau) b_m(0)\rangle \left\langle \exp\left(i\underline{q}\cdot[\underline{r}_m(\tau) - \underline{r}_m(0)]\right)\right\rangle \tag{25}$$

There is no need to satisfy the condition (24) for large $|\Delta\underline{r}_m(\tau)| \gg 1/q$ since in this case the exponential factor gets very small, hence this condition can be replaced by

$$1/q \ll L_{sc}$$

The latter condition is typically satisfied in the DLS experiments. [2] Thus, eq. (23) for the heterodyne correlation function (6) transforms into

$$F_1(\underline{q},\tau) \simeq \langle N\rangle\, F_s(\underline{q},\tau) \tag{26}$$

where we used eqs. (20), (21) and $\langle N\rangle \equiv \langle N(t)\rangle$ is the statistical average of the number of particles in V [1] (note also that $b_m(\tau) = b_m(0)$ for most of the particles since $|\Delta\underline{r}_m(\tau)| \ll L_{sc}$).

From the statistical independence between the scattering particles and between their $\Delta r_m(\tau)$ displacements and $b_m(t)$ values we get for the factor F_2 (cf. eqs. (9), (19)) similarly to eq. (25):

$$F_2(\underline{q},\tau) = \left\langle \sum_m b_m^2(\tau) \times \sum_n b_n^2(0)\right\rangle +$$

$$+ \left\langle \sum_m b_m(\tau)b_m(0) \times \sum_{n\neq m} b_n(\tau)b_n(0)\right\rangle F_s(\underline{q},\tau)F_s(-\underline{q},\tau) \tag{27}$$

Then, using eqs. (18), (20), we obtain:

$$F_2(\underline{q},\tau) = \langle N(\tau)N(0)\rangle + \langle N(N-1)\rangle \left|F_s(\underline{q},\tau)\right|^2 \tag{28}$$

For large systems with $N \gg 1$ particles we can neglect fluctuations of N, hence [1]

$$F_2(\underline{q},\tau) = \langle N\rangle^2 \left[1 + \left|F_s(\underline{q},\tau)\right|^2\right] \tag{29}$$

(the so-called *Gaussian approximation*). In this case the two DLS correlation functions are connected (cf.eqs. (26), (29), (22)):

$$F_2(\underline{q},\tau) - F_2(\underline{q},\infty) = \left|F_1(\underline{q},\tau)\right|^2 \tag{30}$$

The normalized correlation functions, eqs. (14), (16), are connected in a similar way:

$$g^{(2)}(q,\tau) - 1 = \beta\left|g^{(1)}(q,\tau)\right|^2, \qquad \beta = \frac{F_1(q,0)^2}{F_2(q,\infty)} \tag{31}$$

(the so-called *Siegert relation*) [1]. From the definitions eqs. (9), (10):

$$F_2(q,\infty) = \langle c_V(q,0), c_V^*(q,0)\rangle^2 = F_1(q,0)^2,$$

hence $\beta = 1$ for the ideal case considered in the present subsection.

---

[2] In fact, the typical DLS range of wave-vectors is: $0.5\times10^5\mathrm{cm}^{-1} < q < 2\times10^5\mathrm{cm}^{-1}$ (scattering angle $\theta = 30^0 - 150^0$) and the scattering volume linear sizes are $L_{sc} \simeq 0.1 - 1$ mm (Fig. 2), hence $L_{sc}q > 500 \gg 1$.

2.4.b. Identical particles in uniform drift

Let us consider a dilute solution of identical diffusive particles which are forced to move (by an external force and/or a macroscopic flow) with an average velocity $\underline{v}$. Then the particle concentration $c(\underline{r},t)$ follows the diffusion equation with a drift [1]:

$$\frac{\partial c}{\partial t} + \nabla \underline{J} = 0; \qquad \underline{J} = \underline{v}c(\underline{r},t) - D\nabla c(\underline{r},t) \tag{32}$$

where $\underline{J}(\underline{r},t)$ is the particle flux, and D is the diffusion coefficient which is related to the so-called hydrodynamic radius R_H of the particles via the Stokes-Einstein relation:

$$D = \frac{k_B T}{6\pi\eta R_H} \tag{33}$$

where T is the absolute temperature and η is the solvent viscosity. Solving eqs. (32) we get:

$$c(\underline{r},t) = \int F_s(\underline{r}-\underline{r}',t)c(\underline{r}',0)\mathrm{d}^3 r', \tag{34}$$

$$F_s(\underline{r},t) \equiv \frac{1}{(4\pi Dt)^{d/2}} \exp\left(-\frac{(\underline{r}-\underline{v}t)^2}{4Dt}\right) \tag{35}$$

where $d=3$ is the space dimension, and $c(\underline{r}',0)$ is the initial distribution.

The Green function $F_s(\underline{r},t)$ in eq. (34) (also called the Van-Hove space-time correlation function) is a conditional probability to find the particle at the point $\underline{r}$ at time t if initially it was at $\underline{r}=0$ (i.e., for the initial condition $c(\underline{r},0) \equiv \delta(\underline{r})$). Hence $F_s(\underline{r},t)$ simultaneously determines the self-intermediate function $F_s(\underline{q},\tau)$ (cf. eq. (21)) [1]:

$$F_s(\underline{q},\tau) = \int e^{i\underline{q}\cdot\underline{r}}\, F_s(\underline{r},\tau)\mathrm{d}^3 r \tag{36}$$

From eqs. (35), (36) we get for a dilute solution with a drift:

$$F_s(\underline{q},\tau) = \exp(i\underline{q}\cdot\underline{v}\tau)\cdot\exp(-q^2 D\tau) \tag{37}$$

From eqs. (14), (26), (37) we get the function $\Re\left[g^{(1)}(\underline{q},\tau)\right]$ which can be determined in a heterodyne experiment (cf. eq. (15)):

$$\Re\left[g^{(1)}(\underline{q},\tau)\right] = \Re\left[F_s(\underline{q},\tau)\right] = \cos(\underline{q}\cdot\underline{v}\tau)\cdot\exp(-q^2 D\tau) \tag{38}$$

This is an oscillating function with the period

$$T_{\mathrm{osc}} = \frac{2\pi}{\underline{q}\cdot\underline{v}} \tag{39}$$

carrying an information about the value and the direction of the drift velocity $\underline{v}$. The above equations serve as a basis of the laser Doppler velocimetry [24–29].

In contrast to $g^{(1)}$, the homodyne function $g^{(2)}$ normally has a simple exponential shape and does not depend on the drift $\underline{v}$: indeed, for many particles in the scattering volume $\langle N\rangle \gg 1$ eqs. (16), (29), (37) give

$$g^{(2)}(\underline{q},\tau) - 1 = \left|F_s(\underline{q},\tau)\right|^2 = \exp(-2q^2 D\tau) \tag{40}$$

2.4.c. Multicomponent solution (polydisperse scattering objects)

Let us turn to the more general case with several distinct types of scattering particles in the solution contains. The amplitude E of the scattered electric field now is (instead of eq. (4)):

$$E \propto \sum_p M_p c_V^{(p)}(\underline{q},t) \equiv C_V(\underline{q},t) \tag{41}$$

where the summation is taken for all types (p) of the particles, M_p is the material constant characterizing p-particles, and $c_V^{(p)}$ is the Fourier transform of the space distribution of these particles (as defined in eq. (19) with the summation over p-particles only). In analogy with section 2.3, one can show that the homodyne and the heterodyne DLS experiments yield the functions $\Re\left[g^{(1)}\right]$and $g^{(2)}$ defined with eqs. (14), (15), (16) in terms of the respective correlation functions F_1 and F_2 (cf. eqs. (10), (9) with $C_V(\underline{q},t)$ instead of $c_V(\underline{q},t)$). We define also the partial correlation functions:

$$F_1^{(p)}(\underline{q},\tau) \equiv \left\langle c_V^{(p)}(\underline{q},\tau) c_V^{(p)*}(\underline{q},0)\right\rangle \tag{42}$$

$$F_2^{(p)}(\underline{q},\tau) \equiv \left\langle c_V^{(p)}(\underline{q},\tau) c_V^{(p)}(\underline{q},0) c_V^{(p)*}(\underline{q},\tau) c_V^{(p)*}(\underline{q},0)\right\rangle \tag{43}$$

Assuming that the particles are uncorrelated (which is true in a dilute solution), we define a set of self-intermediate scattering functions for each type p (cp. eq. (21)):

$$F_s^{(p)}(\underline{q},\tau) \equiv \left\langle \exp\left(i\underline{q}\cdot[\underline{r}_m(\tau)-\underline{r}_m(0)]\right)\right\rangle \tag{44}$$

where m is a particle of the type p. The arguments of subsection 2.4.a lead to the following 'partial' relations:

$$F_1^{(p)}(\underline{q},\tau) = \langle N_p\rangle\, F_s^{(p)}(\underline{q},\tau) \tag{45}$$

$$F_2^{(p)}(\underline{q},\tau) = \langle N_p\rangle^2 \left[1+\left|F_s^{(p)}(\underline{q},\tau)\right|^2\right] \tag{46}$$

(cf. eqs. (26), (29)) where $\langle N_p\rangle$ is the statistical average of the number of p-particles in the scattering volume V (here we neglect fluctuations δN_p assuming that the scattering volume is large enough, $N_p \gg 1$, which is equivalent to the Gaussian approximation). The total correlation function F_1 of the multicomponent system then is:

$$F_1(\underline{q},\tau) = \sum_p M_p^2 \left\langle c_V^{(p)}(\underline{q},\tau) c_V^{(p)*}(\underline{q},0)\right\rangle = \sum_p \langle N_p\rangle\, M_p^2 F_s^{(p)}(\underline{q},\tau) \tag{47}$$

Turning to the total homodyne correlation function, $F_2(\underline{q},\tau) \propto \langle C^4\rangle$, we note that it is only the terms of type $\left\langle c_V^{(p)} c_V^{(p)*} c_V^{(p')} c_V^{(p')*}\right\rangle$ that survive in F_2 after the averaging (recalling the mutual statistical independence of the particles and that $\left\langle \exp\left(i\underline{q}\cdot\underline{r}\right)\right\rangle = 0$). Hence

$$F_2(\underline{q},\tau) = \sum_p M_p^4 F_2^{(p)}(\underline{q},\tau) + \sum_p \sum_{p' \neq p} M_p^2 M_{p'}^2 \left(F_1^{(p)}(\underline{q},0) F_1^{(p')}(\underline{q},0) + F_1^{(p)}(\underline{q},\tau) F_1^{(p')*}(\underline{q},\tau) \right)$$

Finally, using eqs. (45), (46), (44) we get (recalling that $F_s^{(p)}(\underline{q},0) = 1$):

$$F_2(\underline{q},\tau) = \sum_p \sum_{p'} M_p^2 \langle N_p \rangle M_{p'}^2 \langle N_{p'} \rangle \left[1 + F_s^{(p)}(\underline{q},\tau) F_s^{(p')*}(\underline{q},\tau) \right] \tag{48}$$

Using eqs. (22), (47) we get:

$$F_2(\underline{q},\tau) - F_2(\underline{q},\infty) = \left| \sum_p M_p^2 \langle N_p \rangle F_s^{(p)}(\underline{q},\tau) \right|^2 = \left| F_1(\underline{q},\tau) \right|^2 \tag{49}$$

where

$$F_2(\underline{q},\infty) = \left(\sum_p M_p^2 \langle N_p \rangle \right)^2 \tag{50}$$

These results show that the relationship (30) between F_1 and F_2 stays valid also for polydisperse systems, and the same is true concerning the Siegert relation between $g^{(1)}$ and $g^{(2)} - 1$ (eq. (31)).

Let us now turn to a solution of polydisperse diffusive particles moving with distinct drift velocities $\underline{v}_1$,..., $\underline{v}_p$. The first correlation function, eq. (47), then reads (on using eq. (37)):

$$F_1(\underline{q},\tau) = \sum_p \langle N_p \rangle M_p^2 \exp\left(i\underline{q} \cdot \underline{v}_p \tau - q^2 D_p \tau \right) \tag{51}$$

The heterodyne DLS experiment (see eqs. (14), (15)) allows to obtain $\Re\left[F_1(\underline{q},\tau)/F_1(\underline{q},0) \right]$ which is now a sum of p damped oscillation modes with frequencies ω_1,...ω_p ($\omega_{p'} = \underline{q} \cdot \underline{v}_{p'}$), cf. eq. (39)). The homodyne DLS experiments (see eqs. (16), (49)) measure $(g^{(2)}(\underline{q},\tau) - 1) = \left| F_1(\underline{q},\tau) \right|^2 / F_2(\underline{q},\infty)$ which now includes oscillating terms reflecting all the velocity differences:

$$g^{(2)}(\underline{q},\tau) - 1 = \sum_p \alpha_p^2 \exp(-2q^2 D_p \tau) +$$

$$+2 \sum_p \sum_{p'>p} \alpha_p \alpha_{p'} \exp\left[-q^2 (D_p + D_{p'}) \tau \right] \cdot \cos\left[\tau \underline{q} \cdot \left(\underline{v}_p - \underline{v}_{p'} \right) \right] \tag{52}$$

see eqs. (16), (49). Here α_p is a material constant related to the polarizability of p-particles and their concentration:

$$\alpha_p = \frac{\langle N_p \rangle M_p^2}{\sum_{p'} \langle N_{p'} \rangle M_{p'}^2} \tag{53}$$

For the case of only two distinct types of particles, the heterodyne function $\Re\left[F_1(\underline{q},\tau)/F_1(\underline{q},0) \right]$ consists of just two oscillating terms with frequencies ω_1 and ω_2. Concomitantly, the homodyne function $g^{(2)}(\underline{q},\tau) - 1$ includes only one oscillating term with frequency

$$\omega = |\omega_1 - \omega_2| = \left|\underline{q} \cdot \Delta\underline{v}\right|, \quad \Delta\underline{v} \equiv \underline{v}_1 - \underline{v}_2 \tag{54}$$

With no drift (for pure diffusion) the DLS result, eq. (52), transforms to

$$\sqrt{g^{(2)}(\underline{q},\tau) - 1} = \sum_p \alpha_p \exp(-q^2 D_p \tau) = \int_0^\infty G(\Gamma) e^{-\Gamma\tau} \mathrm{d}\Gamma, \quad \Gamma = q^2 D \tag{55}$$

The integral expression is generally valid for systems of polydisperse scattering objects with different diffusion constants D. Thereby the DLS technique provides information on the size distribution of the scattering objects: the rate Γ reflects the particle size (hydrodynamic radius) R_H (cf. eq. (33)), while the function $G(\Gamma)$ is related to α_p, hence to the partial concentrations N_p/V of the particles (cf. eq. (53); the dependence $R_H(M_p)$ is expected to be known).

To obtain $G(\Gamma)$ based on DLS data an inverse Laplace transform in eq. (55) must be done, which is a difficult problem. It is usually solved using the special regularization programs like the CONTIN algorithm [31,32]. The latter procedure allows to distinguish between two particle populations if their respective rates Γ differ by a factor of 5 or more and the ratio of their intensities $G(\Gamma_1)/G(\Gamma_2)$ is below 10^5.

3. Results: Unusual oscillations in the homodyne DLS correlation function of TAA solutions

TAA self-assembling nanowires is an example of a system with complicated multi-level internal organization. To monitor the size distribution and the growth of the aggregates (fibrils) at various experimental conditions is a challenging task. As explained above, the DLS technique is a suitable tool to deal with this problem (by getting $G(\Gamma)$, cf. eq. (55)). However, the time-dependence of the DLS homodyne correlation functions turned out to be unusual for TAA solutions: it involves well-defined *oscillations* (with more than a dozen periods) of the intensity correlation function $g^{(2)}(\underline{q},\tau)$ in the long time range for all irradiated samples of TAA solutions in chloroform. As shown below, these oscillations cannot be readily explained with the argument which led to eq. (52) due to their unusually *long-lasting* character (see section 4.1 below).

For the purpose of the analysis we fit the time-dependencies of the DLS intensity correlation functions in analogy with eq. (52). It turns out that $g^{(2)} - 1$ shows an initial quasi-exponential decay (with a few relaxation modes) followed by a damped oscillatory relaxation (with a regular period and slow decay) and by the terminal exponential decay at very long times:

$$g^{(2)}(\tau) - 1 \simeq \sum_i G_i \exp(-\frac{\tau}{\tau_i}) + G_{\mathrm{osc}} \exp(-\frac{\tau}{\tau_{\mathrm{osc}}}) \times \cos(\frac{2\pi\tau}{T_{\mathrm{osc}}}) + G_e \exp(-\frac{\tau}{\tau_e}) \tag{56}$$

see the values of the fitting parameters in Table 2. While the *initial* (pre-oscillation) decay generally involves few relaxation modes (with $\tau_i < T_{\mathrm{osc}}$), for the *terminal* decay ($\tau_e > T_{\mathrm{osc}}$) just one mode is typically enough for fitting. The decaying exponents in eq. (56) correspond to diffusion of particles with hydrodynamic radii, R_H, related to the decay time τ:

$$R_H = K \sin^2(\theta/2)\ \tau, \qquad K \equiv \frac{16\pi k_B T}{3\eta}\left(\frac{n}{\lambda}\right)^2 \simeq 0.062\frac{\mathrm{cm}}{\mathrm{s}} \tag{57}$$

(cf. eqs. (3), (33), (52)). Note however, that the fastest modes with $\tau_i < 3\times10^{-7}$s can be excluded from the consideration of the TAA aggregation kinetics as they formally correspond to $R_H < 0.1\,\mathrm{nm}$ (for $\theta = 90^0$), i.e., to submolecular scales.

Our DLS experiments show that self-assembly (induced by white-light irradiation as explained in section 2.1) is a prerequisite for the oscillations in $g^{(2)}$. Typically just a few seconds of irradiation is enough to impart the oscillating character of $g^{(2)}$. For example, Fig. 3 shows the homodyne signal from TAA solutions monitored after short light pulses (irradiation time of t_{irr} =5–15s provides subsequent TAA dark-phase self-assembly within $\lesssim$ 10s [14]). The long-lasting oscillations ($\tau_{\mathrm{osc}}/T_{\mathrm{osc}} \simeq 4$ for t_{irr} =5s and 10s) are apparent for all curves, with a moderate decrease of the periods T_{osc} for longer pulses. For the shortest pulse, t_{irr} =5s, the initial decay contains a few modes related to oligo-aggregates (relaxation rates in the range $2\times10^{-6}\mathrm{s} < \tau_i < 7\times10^{-4}\mathrm{s}$ correspond to $0.6\mathrm{nm} < R_H < 0.22\mu\mathrm{m}$, cf. eq. (57)) pointing to a substantial amount of small aggregates in the TAA solution. Relatively noisy character of the intensity correlation function $g^{(2)}$ for $\tau < 10^{-3}$s reflects the presence of *transient modes* corresponding to growing fibrils with lengths up to 200nm whose concentration changes during 1hour of monitoring in the DLS experiment. However, for longer irradiation times (t_{irr} = 10 and 15s) the submicron aggregates are not detected any more (see Table 2), manifesting a significant growth of the self-assembling TAA fibrils with the irradiation time. In parallel, some micrometric fibers can be seen with the naked eye as they glitter in the laser beam in these solutions. Such changes in the aggregate sizes are in line with the fibril growth behavior reported in ref. [14].

Oscillations with periods $T_{\mathrm{osc}} = 2\pi/\omega_0 \simeq (5.8 - 7.5)$ ms which are observed for the intermediate time-scales ($T_{\mathrm{osc}}/4 < \tau < \tau_e$) formally correspond to frequencies $\omega_0 = q\Delta v$ (cf. eq. (54)) with

$$\Delta v = \frac{\lambda_0}{2n}\frac{1}{T_{\mathrm{osc}}\sin(\theta/2)}, \qquad \frac{\lambda_0}{2n} \simeq 2.2\times10^{-5}\mathrm{cm} \tag{58}$$

(cf. eq. (3)). Hence $\Delta v \simeq 41 - 53\mu$m/s for the three curves of Fig. 3 (we used $\theta = 90^0$ and assumed that $\underline{q}\cdot\Delta\underline{v} = q\Delta v$).

The presence of oscillations in the long-time range of the DLS autocorrelation function $g^{(2)}$ is a well-known phenomenon in systems with strong light absorption where the incident laser beam cause heating of the illuminated part of the solution [15–17]. Indeed, such heating can cause the thermo-gravitational convection in the sample. As the flow velocity $\underline{v}(\underline{r})$ generally depends on the position $\underline{r}$, the particles in different parts of the scattering volume V can move with different drift speeds $\underline{v_p}$ leading to oscillations as described in section 2.4.c (cf. eq. (52)).

The solution of self-assembled conductive TAA fibrils we study is indeed characterized by strong absorption at the laser frequency, see Fig. 1d. One could therefore expect the emergence of a convective flow (due to laser heating) leading to some oscillations in $g^{(2)}$. However, the principal difference between the oscillations in the present system and the previously reported oscillations in the light-absorbing solutions is the *long-lasting character* of oscillations in our case with more than a dozen of periods (see Fig. 3b).

By contrast, a regular convective flow pattern implies that the drift velocities $\underline{v_p}(\underline{r})$ change smoothly in the space. As a result the scattering volume V should contain particles with different drift velocities giving rise to a superposition of oscillating terms with different periods in $g^{(2)}$. An analysis [15,33] (see also section 4.1 below for details) shows that in such situations the amplitude of oscillations in the autocorrelation function $g^{(2)}$ rapidly decay with time τ, in contradiction to the behavior of our system (a comparison is presented below in Fig. 12).

In order to clarify the origin of the oscillations we performed a detailed experimental investigation of this phenomenon. The list of the main experiments can be found in Table 1. Most of them were done at the maximum laser power $P_0 = 21-22$mW which ensures the best signal-to-noise ratios. In each experiment we monitored the initial laser power P_0 (at point '0', see Fig. 2), the fraction $P_2/P_2^{\rm tol}$ of the light power left in the beam after passing through the sample (at point '2'), and the relative intensity of the scattered light, $I_3/I_3^{\rm tol}$ (at point '3' corresponding to scattering at $\theta = 90^0$). [3] The well-defined oscillations in the function $g^{(2)}$ were detected at long times in all *irradiated* samples of TAA chloroform solutions for all concentrations studied (ranging from 0.375 to 7.5mM, or 0.023-0.45 vol%). On the contrary, no oscillations were found in non-irradiated samples. Table 1 also shows the values of the oscillation period $T_{\rm osc}$ (cf. eq. (56)) in the cases when oscillations in $g^{(2)}(\tau)$ were visible in time range $10^{-3}{\rm s} < \tau < 10^{-1}{\rm s}$.

We also observed the following interesting phenomenon: as soon as the sample was illuminated with white light for a few seconds, the laser beam start to shift vertically downwards (see Figure 4), while the solution starts to visibly absorb the laser light. Within the first minute after switching-on the laser the incident beam progressively deflects downwards and often form an interference ring pattern [34] behind the sample. The maximal vertical shift (after stabilization of the pattern) for the 7.5 mM solution irradiated for 1 hour corresponds to an angle $\theta_\perp^{(0)} \simeq 0.02$ for the centre of the beam and up to $\theta_\perp^{(r)} \simeq 0.045$ for the diffraction cone pattern around the central spot (see Table 1). For briefly irradiated solutions (like 5s irradiation followed by incubation in the 'dark' when only the DLS red laser light is applied) we detected a smaller vertical shift with $\theta_\perp^{(0)} \simeq 0.004$ and no apparent diffraction pattern.

Although the appearance of irradiated for 5s and then incubated TAA solutions is very similar to that of the original monomeric solution (lightly yellow and transparent), such solutions do absorb and scatter laser light, and the absorbance increases with the incubation time t_{inc} (see Table 1 for the transmitted light intensity, $P_2(t_{inc})$, for 7.5mM solution incubated in the dark for time t_{inc} after irradiation for 5s). By contrast, the solutions irradiated for 1h manifest the maximum absorbance which slowly decreases during the incubation time (compare 7.5mM solutions with $t_{irr} = 1$h and $t_{inc} = 0 - 19$h). Concomitantly, they change color from brightly green to brownish (cf. the absorbance plot in Fig. 1d).

While the period of oscillations strongly depends on the irradiation time (e.g. $T_{\rm osc} \sim 7 \times 10^{-3}$s for 7.5mM TAA solutions for $t_{irr} = 5$s, and $T_{\rm osc} \sim 2.5 \times 10^{-3}$s for

---

[3] The intensity values P_2 and I_3 are normalized by the respective intensities, $P_2^{\rm tol}$ and $I_3^{\rm tol}$, measured for pure toluene using the same laser power P_0.

$t_{irr} = 1$h right after irradiation), it rather weakly depends on the incubation time in the dark (slowly increasing with t_{inc} up to $T_{\rm osc} \simeq 8.5 \times 10^{-3}$s for $t_{irr} = 5$s, and up to $T_{\rm osc} \simeq 3.5 \times 10^{-3}$s for $t_{irr} = 1$h after $t_{inc} = 19$h), see Figures 5a,b and Table 1. Moreover, the oscillations become faster at higher concentrations (see Figure 6). These observations are in accord with the expected variations of the laser light absorption: it increases at higher concentrations and for longer irradiation time, but becomes weaker with longer incubation time t_{inc}.

Following the literature reports on $g^{(2)}$ oscillations caused by light absorbance [9,15,16,33,35] we studied the influence of the scattering angles θ on the intensity correlation function $g^{(2)}$. As the oscillations are observed at any concentration, dilute TAA solutions ($c = 0.375$mM) were used in order to minimize the absorption of the laser beam and hence to weaken the dependence of the scattered intensity I_3 on the position of a scattering element along the incident laser beam. We used long-irradiated samples ($t_{irr} = 1$hour) and maximal laser intensity (22.2mW). To minimize the effect of the incubation time variation, we considered just 3 different scattering angles ($\theta = 60^0$, 90^0 and 120^0) for most of the series, and made each series of measurements within 12min time-lags (three measurements of $t_{DLS} = 200$s and 1-2mins for an adjustment of the scattering angle θ). The auto-correlation functions $g^{(2)}(q, \tau)$ for these three angles θ were recorded roughly every hour during the first 3 hours of the 'dark incubation' after the irradiation. For all these series, no dependence of the period T_{osc} on the scattering angle θ was observed, while a weak but detectable changing in the oscillation period was registered over the course of this experiment (cf. Table 1). Finally, the conclusion that $T_{osc}(\theta) = \text{const}$ was confirmed by the functions $g^{(2)}(q, \tau)$ recorded for the scattering angles between 30° and 140° (with 12 different θ) after $t_{inc} = 3$h30min-4h05min incubation in the dark, see Figure 7 and 9c. This is in contrast with previous reports on light-absorbing assemblies and polymers where a clear dependence of the oscillation period on the scattering angle was observed [15,16].

Given that light absorption leads to a local heating and convection, it is essential to establish the effect of the incident laser light power P_0. When recording the DLS data at a fixed scattering angle ($\theta = 90^0$) for TAA solution, $c = 0.375$mM, illuminated for $t_{irr} = 1$ hour and kept in the dark for $t_{inc} = 5$ hours prior to the measurement, we found that a variation of the incident laser power results in a change of the oscillation period (see Figure 8 and Tables 1, 2). The oscillations were shown to shift to slower times as the laser power decreases. At the same time the amplitude of the oscillatory mode (with $T_{\rm osc}$ between $\simeq 6 \times 10^{-3}$ and 4×10^{-2}s) decreases making it easier to separate from the fast decay modes (with τ_i) associated with diffusion of short fibril fragments.

The dependencies of the oscillation period $T_{\rm osc}$ on various experimental parameters (TAA concentration c, incident laser power P_0, white-light irradiation time t_{irr}, incubation time t_{inc} in the 'dark', and the scattering vector q) are summarized in Fig. 9.

In addition, we have examined the effect of fibril size on the period $T_{\rm osc}$ (which is possibly related to sedimentation of self-assembling aggregates). To this end, two sonication experiments were performed. In the first experiment two aged self-assembled TAA solutions with $c = 0.375$mM and $c = 7.5$mM (which were prepared by irradiation for $t_{irr} = 1$h followed by incubation in the dark for $t_{inc} = 42$h) were

sonicated for 2 hours in the dark. The correlation functions $g^{(2)}$ were recorded just before the sonication (at $t_{son} = 0$) and then every 30min during the sonication stage, and finally 3 hours after the end of sonication (i.e., at $t_{son} + t_{rest}$ with $t_{son} = 2\text{h}$ and $t_{rest} = 3\text{h}$). The results are shown in Fig. 10. The DLS recording times were chosen here to be very short (20s) in order to avoid re-assembling of the aggregates during the DLS measurements when the sonication was temporary interrupted for instrumental reasons (on the adverse side, the shorter measurement time is responsible for a higher noise level in the DLS signal). We observe that the resulting period T_{osc} is nearly the same for all measurements.

Another sonication experiment was done with freshly prepared 0.375mM TAA solution which was simultaneously sonicated and irradiated with white light during 1 hour. Every 10 mins the sonication/irradiation was interrupted for 10s for brief DLS recording. The results are presented in Fig. 11. The oscillation period slightly decreases from $T_{\text{osc}} \simeq 8 \times 10^{-3}\text{s}$ for the first record (at $t_{son} = 10\text{min}$) to $T_{\text{osc}} \simeq 6 \times 10^{-3}\text{s}$ at $t_{son} \geq 30\text{min}$, and then it stabilizes.

4. Discussion

The regular oscillations observed in the intensity correlation function $g^{(2)}$ may arise from the so-called 'heterodyning' of the scattered light when the detector simultaneously receives light scattered from two (or more) distinct scattering objects moving with different drift velocities v_1 and v_2, cf. eqs. (52), (54). As such objects one can consider solute particles in separate subvolumes V_1 and V_2 (both belonging to the scattering volume) having distinct macroscopic drift velocities v_1 and v_2, or two distinct species in a common volume (e.g. small particles and large aggregates) whose motion with distinct velocities is driven by an external force field.

The two possibilities are considered in references [15,16]. In the first reference, Schaertl and Roos proposed an inhomogeneous convection pattern due to local heating of dispersed gold clusters by the incident laser beam: the convection flux velocity changes from $-v$ to $+v$ near the center of the beam inside the scattering volume. In the next section 4.1 we shall consider a generalization of this model for an arbitrary experimental geometry (the shape of the scattering volume and the flow pattern in the solution) trying to explain the intermediate and long-time oscillations in the $g^{(2)}$ function.

In the second reference, Sehgal and Seery introduced a model where the heavy and the light fractions of the solute (composed of light absorbing polyaniline or complexes of cytochrome c and cytochrome c peroxidase) are moving with distinct velocities $v_1 \neq v_2$ due to a local gradient of macroscopic flow field. It leads to the following autocorrelation function (the oscillatory relaxation model):

$$g^{(2)}(\underline{q},\tau) - 1 = A_1 \exp\left[-2q^2 D_1 \tau\right] + A_2 \exp\left[-2q^2 D_2 \tau\right] +$$

$$+ A \exp\left[-q^2(D_1 + D_2)\tau\right] \cdot \cos(\underline{q} \cdot \Delta\underline{v}\tau), \tag{59}$$

where $\Delta\underline{v} = \underline{v}_1 - \underline{v}_2$.

4.1. A quantitative description of convection-related DLS oscillations.

Let us consider a solution with just one type of solute particles characterized by the same diffusion coefficient D. In the presence of a convection flow the particles move with different drift velocities $\underline{v} = \underline{v}(\underline{r})$ depending on the particle position $\underline{r}$. In this case eq. (52) transforms as:

$$g^{(2)}(\underline{q},\tau) - 1 = A \exp(-2q^2 D\tau)\ \tilde{g}(\underline{q},\tau), \tag{60}$$

$$\tilde{g}(\underline{q},\tau) = \frac{1}{V^2} \int_V \mathrm{d}^3 r \int_V \mathrm{d}^3 r' \cos\left[\tau \underline{q} \cdot (\underline{v}(\underline{r}) - \underline{v}(\underline{r}'))\right] \tag{61}$$

where we assume that the average concentration of particles, $c(\underline{r})$, is the same everywhere within the scattering volume V. The oscillations smear out at longer time τ. Mathematically it is similar to the smearing of the intensity oscillations in the diffraction pattern from a hole at large diffraction angles [33]. The smearing depends on the geometry of the scattering volume V and the distribution of the drift velocities $\underline{v}(\underline{r})$ in it.

The simplest assumption is that the drift velocity changes linearly in space, hence so does $\underline{q} \cdot \underline{v}(\underline{r})$ (say, it varies from a_1 to a_2 in the scattering volume). As a result, the cosine argument τX, $X = \underline{q} \cdot (\underline{v}(\underline{r}) - \underline{v}(\underline{r}'))$, should vary within the segment $[-\tau\omega, \tau\omega]$, with $\omega = a_2 - a_1$. Depending on the geometry of the scattering volume V, the integration of $\cos(\tau X)$ in eq. (61) results in

$$\tilde{g}_1(\omega\tau) = \left[\frac{\sin(\omega\tau)}{\omega\tau}\right]^2 \qquad \text{for slit aperture} \tag{62}$$

$$\tilde{g}_2(\omega\tau) = \left[\frac{2J_1(\omega\tau)}{\omega\tau}\right]^2 \qquad \text{for cylindrical aperture} \tag{63}$$

$$\tilde{g}_3(\omega\tau) = 9\left[\frac{\sin(\omega\tau)}{(\omega\tau)^3} - \frac{\cos(\omega\tau)}{(\omega\tau)^2}\right]^2 \qquad \text{for spherical aperture} \tag{64}$$

where J_1 is the Bessel function of the first kind and first order. The equations above correspond to the three most natural geometries of the scattering volume. The 'cylindrical' aperture means that the volume V is cylindrical along the beam and that the drift velocity $\underline{v}$ changes in a linear fashion across this volume (i.e., in the direction perpendicular to its axis). This situation is quite natural for a laser beam; it was considered in ref. [15]. The 'spherical' aperture means that the scattering volume V is restricted equally in all three directions (so that V is spherical). By contrast, the 'slit' geometry means that all cross-sections of the volume V along the planes of equal velocities (with the same value of $\underline{q} \cdot \underline{v}(\underline{r})$) have equal areas. This situation can be realized for a laser beam of uniform thickness if the drift velocity changes along the beam (but not across it).

The smearing functions, eqs. (62), (63), (64) (see Fig. 12b) are universal functions of the renormalized time parameter $\omega\tau$. They determine the time-decay character of the oscillations in the autocorrelation function $g^{(2)}$. The slit model

(eq. (62)) gives the slowest decay, whereas the spherical aperture model (eq. (64)) provides the fastest smearing of the oscillations. Note that the full auto-correlation function $g^{(2)}$, eq. (60), includes also the exponential factor whose decay is defined by an independent parameter q^2D.

The theoretical predictions given in eqs. (60), (61) are compared in Fig. 12a with the experimentally obtained correlation functions $g^{(2)}$. The weakest theoretical damping corresponds to the absence of diffusion ($D = 0$, $g^{(2)}(\underline{q},\tau) - 1 \propto \widetilde{g}(\underline{q},\tau)$) and to the 'slit' geometry: $\widetilde{g} = \widetilde{g}_1$, eq. (62). Hence,

$$g^{(2)}(\underline{q},\tau) - 1 = A \left[\frac{\sin(\omega\tau)}{\omega\tau}\right]^2 + A_0 \tag{65}$$

where $\omega = \omega(\underline{q})$, $\omega \equiv \left[\underline{q}\cdot\underline{v}(\underline{r})\right]_{\max} - \left[\underline{q}\cdot\underline{v}(\underline{r})\right]_{\min}$ (the minimal and maximal values within the scattering volume) and A_0 is a constant related to the background noise and slow processes (with $\tau_{\rm slow} \gg \tau$). However even in this case the data cannot be fitted satisfactorily using the model, eq. (65): experimental oscillations demonstrate substantially weaker damping than any of the 'diffraction' functions, eqs. (62), (63), (64). For the theoretical functions, the ratios of the amplitudes of the first to the second peak and of the first to the fifth peak are $r_{12} \sim$ 2.9-5.9 and $r_{15} \sim$ 14-100 , respectively, whereas the experimental data imply $r_{12} \sim$ 1.2-1.5 and $r_{15} \sim$ 2.2-4.8 .

Such anomalous persistence of oscillations in $g^{(2)}$ from TAA solutions indicates that the observed effect cannot be attributed to convection flow gradients. Rather it may be due to a superposition of signals from two *distinct* scattering sources (either subvolumes or solute components) characterized by well-defined but distinct drift velocities. In this case we return to the oscillatory relaxation model, eq. (59), which indeed provides a good fit of the experimental data (cf. Figs. 3, 12a). [4] However, it is unlikely that the scattering volume involves two subvolumes with different macroscopic velocities, v_1 and v_2, and that no intermediate velocities are present there. Thus, we are driven to consider the last option: that there are *two distinct components* moving with different velocities in the solute. In the next sections we discuss this possibility in detail, in particular we consider the nature of these distinct species, the origin of their drift, its direction and the possible drift patterns in the sample.

4.2. The main prerequisites for $g^{(2)}$-oscillations: sedimentation or convection?

The discussion above makes it clear that the observed oscillations in $g^{(2)}(\tau)$ are likely to be due to *two sorts* of scattering particles moving with distinct velocities, $\underline{v}_1$ and $\underline{v}_2$. The relevant effective drift velocity

$$v^* = \lambda_0/T_{\rm osc} \tag{66}$$

---

[4] Note that eq. (56) is equivalent to eq. (59) as long as the oscillatory part of the DLS correlation function $g^{(2)}(\tau)$ is concerned.

is related to $\Delta\underline{v} = \underline{v}_1 - \underline{v}_2$. [5] Its dependence on various parameters is shown in Fig. 9. Typically $v^* \simeq 50 - 250$ μm/s in our experiments.

Before turning to a discussion on the nature of such two species, let us consider the origin of their assumed coherent motion. Such motion can arise, for example, from sedimentation or convection.

In the case of sedimentation, such collective drift would be rapid enough to be observable by naked eye: for a typical DLS experiment lasting for $t_{DLS} \sim 1$ hour (cf. Fig. 3 showing $T_{\rm osc} \sim 7$ ms) the expected particle displacement is $\Delta v\, t_{DLS} \sim 20$cm, which is much longer than the sample size. Moreover, some TAA samples were incubated for many hours (see Table 1), but no sedimentation was ever detected in the solutions. Furthermore, the DLS experiments were also performed on TAA solutions sonicated in the dark for 2 hours to cut/shorten the TAA fibrils and destroy their large aggregates. The sonication therefore must diminish or suppress the hypothetical sedimentation effect: one can expect that the sedimentation speed should decrease after sonication. However, the sonicated samples still display the characteristic oscillations with nearly the *same* period (Fig. 10) or even *shorter* period corresponding to a faster Δv (Fig. 11).

Therefore, it is the convection that should be favored as a possible reason for oscillations. A thermal convection is expected here since the studied TAA solutions absorb laser light rather strongly due to conductive (metallic) nature of TAA aggregates (typically with 20-50% of laser power absorbed in the samples, see Table 1). The light energy serves to heat the solution locally (around the laser beam) thus reducing its density and inducing gravitational flow as shown schematically in Fig. 13: the flow is directed mainly upward in the beam region. This convection flow is considered in more detail in the next section 4.3 (its velocity is also estimated there).

Eq. (54) shows that the frequency of oscillations, $\omega = \left|\underline{q} \cdot (\underline{v}_1 - \underline{v}_2)\right|$, depends on the scattering vector and velocity orientations. For example, let us assume that the scattering species 1 are convected with velocity $\underline{v}_1 = \underline{v}$, while there is not drift for species 2 ($v_2 = 0$). Then $\Delta\underline{v} = \underline{v}_1 - \underline{v}_2 = \underline{v}$,

$$\omega = \left|\underline{q} \cdot \Delta\underline{v}\right| = \left|\underline{q} \cdot \underline{v}\right| \tag{67}$$

If the scattering vector $\underline{q} = \underline{k}_2 - \underline{k}_1$ is horizontal (which is the standard case in DLS, cf. Fig. 2), the relevant velocity component is also horizontal. By symmetry the horizontal projection of $\underline{v}$ is expected to be parallel to the incident beam ($\underline{k}_1$). Hence $\omega = |(\underline{k}_2 - \underline{k}_1) \cdot \underline{v}| = kv\,(1 - \cos\theta)$, so it must strongly depend on the scattering angle θ. Such dependence, however, was not observed: rather, $\omega = 2\pi/T_{\rm osc}$ is found to be nearly independent of θ (see Fig. 9c). This observation suggests that the scattering vector $\underline{q}$ has a permanent vertical component q_z (independent of θ) and that $\underline{v}$ is nearly vertical: $\underline{v} = v\underline{n}_z$ ($\underline{n}_z$ is vertical unit vector).

While the vertical drift velocity in the scattering volume is pretty compatible with the thermal convection flow pattern (cf. Fig. 13 and the next section), it is less clear how a nonzero q_z can emerge. Here we see 2 possibilities. One way to

---

[5] The effective drift velocity v^* corresponds to $n\Delta\underline{v} \cdot \underline{q}/k$ in eq. (59). As before, $k = 2\pi n/\lambda_0$ is the wavenumber, $n \approx 1.45$ is the refractive index of the solution, cf. eq. (3).

get $q_z \neq 0$ is simply via a not precise alignment of the DLS setup allowing for a small angle between the direction of the scattered light and the true gravitation horizontal plane. [6] Another possibility is related to thermal refraction of the main laser beam downwards due to temperature gradient in the vertical direction, cf. Fig. 4.

Let us first consider the possibility of a non-perfect orientation of the optical table (with unit normal vector $\underline{n}_{DLS}$) with respect to the gravitation vertical direction $\underline{n}_z$. Indeed, due to the DLS set-up alignment procedure, the wave-vector of the primary beam $\underline{k}_1$ and the scattered light wave-vector $\underline{k}_2$ lay perfectly in the DLS set-up plane, i.e.

$$\underline{k}_1 \cdot \underline{n}_{DLS} = \underline{k}_2 \cdot \underline{n}_{DLS} = 0 \tag{68}$$

cf. Fig. 2. Now suppose this plane is tilted with respect to the horizon: $\underline{n}_z \cdot \underline{n}_{DLS} = \cos\gamma < 1$, where the tilt angle γ between $\underline{n}_{DLS}$ and the vertical direction (unit vector $\underline{n}_z$) is small: $\gamma \ll 1$. Choosing the Cartesian coordinate system with z-axis along $\underline{n}_z$ and y-axis perpendicular to both $\underline{n}_z$ and $\underline{n}_{DLS}$, so that $\underline{n}_{DLS} = (\sin\gamma, 0, \cos\gamma)$, we find:

$$\omega = \left|\underline{q} \cdot \underline{v}\right| = \left|(\underline{k}_2 \cdot \underline{n}_z - \underline{k}_1 \cdot \underline{n}_z)\, v_z\right| = k\gamma v_z \left|\sin(\varphi_1 + \theta) - \sin\varphi_1\right| \tag{69}$$

where φ_1 is the angle between the incident beam and the y-axis. For any value of φ_1 the frequency $\omega = \omega(\theta)$ strongly depends on θ. In particular, as θ is varied in the experimental range $30° \leq \theta \leq 150°$ (cf. Fig. 9c), ω must vary at least by a factor of 2. Obviously, such strong angular dependence of ω contradicts the data of Fig. 9c showing that $T_{\rm osc} = 2\pi/\omega$ is practically constant with less than 10% deviations. Hence, the effect of deviation from horizontality of the DLS setup can be neglected.

The remaining second possible reason for $q_z \neq 0$ is the thermal refraction of the main laser beam: the solution is strongly heated right above the beam (due to light absorption and convection), while below it the heating effect is much weaker due to low thermal conductivity of the solution and significant upward convective flow (see Fig. 13). The laser-induced heating thus leads to a strong refractive index gradient, $\mathrm{d}n/\mathrm{d}z < 0$, near the beam. The gradient must give rise to a vertical downward deflection of the beam as it passes through the sample (cf. Fig. 4), showing the so-called thermal lensing effect. Such deflection was indeed observed in most experiments on irradiated TAA solutions, cf. section 3. The typical deflection angles are between $\theta_z \simeq 0.004$ (for briefly irradiated TAA samples, $t_{irr} = 5$s, which were then incubated for 1 hour to accomplish the fibrillization) and $\theta_z \simeq 0.02$ for the 7.5 mM TAA solution irradiated for 1 hour (the case of maximum absorption). As a result, the wave-vector $\underline{k}_1$ of the primary beam tilts down, $k_{1,z} = -k\theta_z$, while the scattered light ($\underline{k}_2$) remains perfectly horizontal (due to alignment of the DLS set-up). Hence, $q_z = k_{2,z} - k_{1,z} = k\theta_z$, and there is no angular dependence of the oscillation period $T_{\rm osc} = 2\pi/\omega$ any more:

---

[6] The DLS set-up is routinely checked for the quality of alignment (which should be parallel to the optical table). However, a verification of horizontality of the table as such is not included in the protocol.

$$\omega = v_z q_z = v_z k \theta_z, \qquad T_{\rm osc} = \frac{\lambda_0}{n v_z \theta_z} \tag{70}$$

4.3. The convection flow pattern

Eq. (67) with vertically oriented $\underline{v}$ gives $\omega = q_z v_z$, hence the dependence of the oscillation frequency ω on the parameters is primarily defined by the convection velocity v_z near the beam. To figure out the convection flow field, we adopt a simplified model assuming an infinite sample size along the vertical axis (z-axis), which is reasonable since the sample height ($\simeq$ 5cm) is much larger than its radius $R = 2.5$mm (R is half of the diameter of the scattering cell). We also assume that the flow is uniform along the beam (x-axis), with 2-dimensional velocity in yz plane (Fig. 13). Thus, we consider a thermo-gravitational convection flow in a slit ($-R < y < R$) rather than in a cylindrical cell. The main goal here is to estimate the convection velocity v_z in the scattering volume, near the origin $y = z = 0$ corresponding to the center of laser beam. The beam diameter $d_{beam} \approx 100\mu m \ll R$. The flow field presumably involves 2 convection rolls extending up to the height $\sim H$ above the beam and on the distance $\sim R$ below it (cf. Fig. 13).

To established the convection flow, we need to consider simultaneously 2 fields: velocity $\underline{v}(\underline{r})$ and temperature $T(\underline{r})$, or $\Delta T(\underline{r}) = T(\underline{r}) - T_{out}$, where T_{out} is the temperature in the bath outside the sample. The temperature rise ΔT is generated by the laser light energy absorption with rate $\sigma_0 I$ per unit volume, where $I = I(\underline{r})$ is the beam intensity and σ_0 is the absorption coefficient. The absorbed heat then propagates outside the beam by convection and thermal diffusion according to the master thermo-conductivity transport equation:

$$\frac{\partial T}{\partial t} + \underline{v} \cdot \nabla T = D_T \nabla^2 T + \sigma_0 I / C_p \tag{71}$$

where $D_T = \lambda_T / C_p$ is the thermo-diffusion constant, λ_T is thermal conductivity of the solution, C_p is its heat capacity per unit volume and $\partial / \partial t$ is time-derivative which is set to 0 below as we consider a stationary flow. The flow velocity is governed by the Navier-Stokes equations with kinematic viscosity $\nu = \eta / \rho_0$, where η is the shear viscosity of the solution and ρ_0 is its density:

$$\frac{\partial \underline{v}}{\partial t} = -\frac{\nabla \Pi}{\rho_0} + \frac{\underline{f}}{\rho_0} + \nu \nabla^2 \underline{v} \tag{72}$$

where Π is excess local pressure equal to the difference between the true pressure and the ideal pressure in the liquid at rest without heating: $\Pi = \Pi_{true} + \rho_0 g z$. The volume force $\underline{f}$ here is the buoyant force (directed upwards) due to temperature expansion of the liquid, $\underline{f} = f_b \underline{n}_z$, with

$$f_b = -\Delta \rho g \simeq \varkappa \rho_0 g \Delta T \tag{73}$$

where $\Delta \rho \ll \rho_0$, g is the gravity acceleration and $\varkappa \approx 1.27 \cdot 10^{-3}$ 1/K is the thermal expansion coefficient of the solvent (chloroform).

The TAA solutions we consider are rather dilute (solute volume fraction $\phi \lesssim 0.5\%$), hence it is possible to approximate their density, heat capacity, thermal conductivity and viscosity by the pure solvent values (at 20°C):

$$\rho_0 \approx 1.49 \frac{\mathrm{g}}{\mathrm{cm}^3}, \quad C_p \approx 1.43 \times 10^7 \frac{\mathrm{erg}}{\mathrm{cm}^3 \cdot \mathrm{K}}, \quad \lambda_T \approx 0.13 \times 10^5 \frac{\mathrm{erg}}{\mathrm{s} \cdot \mathrm{cm} \cdot \mathrm{K}}, \quad \eta \approx 0.57\mathrm{cP} \tag{74}$$

Hence $D_T \approx 9 \cdot 10^{-4} \mathrm{cm}^2/\mathrm{s}$ and $\nu \approx 4 \cdot 10^{-3} \mathrm{cm}^2/\mathrm{s}$ meaning that heat diffusion is slow as compared with vorticity diffusion: $D_T \ll \nu$. In addition, we adopt the following conditions (verified at the end) to simplify the model:

$$D_T \ll R v_0, \qquad R^2 v_0 \ll \nu H \tag{75}$$

where v_0 is the characteristic flow velocity.

The buoyant force (73) driving the flow is defined by the temperature field $T(y,z)$ which is described below. We first focus on the region near the origin, $|y| \ll R$. Here the flow velocity $\underline{v}$ must be directed vertically (along z-axis), $\underline{v} \approx v_0(z)\underline{n}_z$, where the subscript '0' indicates that $y = 0$. Then eq. (71) gives in the stationary case ($\partial T/\partial t \equiv 0$)

$$v_0 \frac{\partial T}{\partial z} = D_T \nabla^2 T + \frac{\sigma_0 I(r)}{C_p} \tag{76}$$

where $\nabla^2 T = \frac{\partial^2 T}{\partial z^2} + \frac{\partial^2 T}{\partial y^2}$. It is useful to recall that the beam intensity is localized in the region $r \equiv \sqrt{y^2 + z^2} \lesssim d_{beam}$: $I(r)$ is negligible for $z \gg d_{beam}$. In this regime eq. (76) is analogous to a simple diffusion equation (with z/v_0 playing the role of time). Assuming that $v_0(z) \approx \mathrm{const}$ (cf. eq. (85) below) and neglecting the term $\partial^2 T/\partial z^2$ in $\nabla^2 T$, the solution of eq. (76) for $z \gg d_{beam}$ reads:

$$\Delta T(y,z) \simeq \frac{\widetilde{W}}{\sqrt{2\pi\sigma_y^2}} \exp\left(-\frac{y^2}{2\sigma_y^2}\right), \qquad \sigma_y^2 \equiv 2D_T z/v_0 \tag{77}$$

where

$$\widetilde{W} = \frac{\sigma_0 P}{v_0 C_p} \tag{78}$$

and

$$P = \int I(\underline{r}) \mathrm{d}y \mathrm{d}z \tag{79}$$

is the total laser power. Here we take into account that $\Delta T \approx 0$ below the beam ($z < 0$, $|z| \gg d_{beam}$) where $T \approx T_{out}$.

Now we note that the term $\partial^2 T/\partial z^2$ can be neglected in eq. (76) if $\sigma_y \ll z$ which is equivalent to $z \gg D_T/v_0$ (we used here the solution, eq. (77)). This condition can be understood with a simple scaling argument. For a given distance z from the beam center, the characteristic drift time is $|z|/v_0$ and the thermo-diffusion time is z^2/D_T (cf. eq. (71)). Therefore the drift dominates over diffusion in z-direction if

$$z \gg z_D \equiv D_T/v_0 = v_0 \tau_D, \qquad \tau_D \equiv D_T/v_0^2 \tag{80}$$

which coincides with the stated above condition to neglect the term $\partial^2 T/\partial z^2$ in eq. (76).

More general results on the temperature field, $\Delta T(y,z)$, are outlined in the Appendix A. The predictions, eqs. (77), (A9), (A11), (A12), are important. They show that the heating effect is localized above the beam in a zone $|y| \lesssim \sigma_y \sim \sqrt{z z_D}$ which is narrow as long as $\sigma_y \ll R$. The latter condition is satisfied if

$$z \ll H \sim R^2/z_D \tag{81}$$

Hence, eqs. (77), (A9) are valid for $z_D \ll z \ll H$. For $z \sim H$ the laser-induced heat is spread over the whole cross-section of the sample and get absorbed by the sample walls. As a result both ΔT and the velocity field decay exponentially for $z \gg H$ (hence, of course, $v_0(z)$ is not constant any more in this regime). Therefore, the length H can be indeed considered as the effective height of convection roll. Note that $H \gg R$ due to the first condition (75). Note also that the mean temperature increment at a height z above the beam, $z_D \ll z \ll H$ is

$$\Delta T_{mean}(z) \equiv \frac{1}{2R}\int \Delta T(y,z)\mathrm{d}y = \frac{\sigma_0 P}{2v_0 C_p R} = \frac{\widetilde{W}}{2R} \tag{82}$$

i.e. it does not depend on the coordinate z (we used here eqs. (77), (78)).

Eq. (77) shows that the force $f_b(y,z) \simeq \varkappa \rho_0 g \Delta T$ driving the flow (cf. eq. (73)) is localized near the xz plane in a significant region of the sample (for $0 < z \ll H$, $H \gg R$). Therefore the force f_b can be replaced by the surface forces $2F_b$ applied at $y = 0$ with

$$F_b = \int_0^R f_b(y,z)\mathrm{d}y$$

Using eq. (77) we find that F_b does not depend on z for $z \gg z_D$:

$$F_b \simeq \frac{1}{2}\widetilde{W}\varkappa\rho_0 g \equiv F_b^0, \qquad z_D \ll z \ll H \tag{83}$$

By contrast, this force is exponentially small below the beam, $z < 0$, $|z| \gg z_D$ (cf. eq. (A11)):

$$F_b \simeq F_b^0 \exp\left(-|z|/z_D\right), \quad z < 0 \tag{84}$$

The uniform surface force $2F_b^0$ above the beam applied at $y = 0$ must naturally generate two unidirectional simple shear flows on both sides of the zx plane (for $y < 0$ and $y > 0$). Assuming the no-slip boundary condition at the solid surfaces: $\underline{v} = 0$ at $y = \pm R$, we get the velocity profile ($\underline{v}$ is directed vertically):

$$v_z(y,z) \simeq \frac{F_b^0}{\eta}\left(R - |y|\right), \quad -R < y < R, \quad R \ll z \ll H \tag{85}$$

The above velocity profile (85), however, violates the volume conservation (incompressibility) condition in the convection slit demanding that

$$\int_{-R}^{R} v_z(y,z)\mathrm{d}y = 0 \tag{86}$$

Physically this condition is provided by an appropriate pressure gradient $\Pi' = \partial\Pi/\partial z$ generating a two-dimensional analogue of the Poiseuille flow (with $\partial^2 v_z/\partial y^2 = \Pi'/\eta$, cf. eq. (72)). Thus, the total velocity becomes

$$v_z \simeq \frac{F_b^0}{\eta}\left(R - |y|\right) + \frac{\Pi'}{2\eta}\left(y^2 - R^2\right) \tag{87}$$

where we used the boundary condition $v_z(\pm R) = 0$ and the symmetry of the flow in the slip $-R < y < R$. From the condition (86): $\Pi' = 1.5F_b^0/R$ yielding

$$v_z \simeq v_0(1 - |y|/R)\,(1 - 3\,|y|/R)\,, \quad v_0 \equiv \frac{RF_b^0}{4\eta}, \quad R \ll z \ll H \tag{88}$$

Note that flow velocity in the specified region does not depend on z, and that it is directed upwards near the center (for $|y| < R/3$) and downwards at the periphery of the sample forming the pattern shown in Fig. 13. Using eqs. (78), (83), (88)) we find

$$v_0 \simeq \left(\frac{\varkappa\rho_0 g}{8\eta C_p}\sigma_0 P R\right)^{1/2} \tag{89}$$

The resulting v_0 is the vertical convection velocity in central part of the flow (for $y \ll R$, $R \ll z \ll H$). For $z \lesssim R$ the flow velocity slightly decreases due to the virtual absence of the buoyant force below the beam (cf. eq. (84)). This effect is neglected in the present study. It is important to note, however, that generally the vertical velocity $v_0 = v_0(y, z)$ changes very little in the region of interest, $|z| \ll R$, $|y| \ll R$, and this feature justifies the assumption $v_z(y, z) = v_0 = \text{const}$ introduced before eq. (77) and used to derive eqs. (77), (A7).

To estimate the numerical value of $v_z = v_0$, eq. (89), we now need to know how the product $\sigma_0 P$ depends on the solution concentration c and the incident laser power P_0. The corresponding analysis can be found in Appendix B, see eq. (B6). The result is

$$\sigma_0 P \simeq \beta\widetilde{\beta}\alpha c P_0 \exp(-\alpha c R) \tag{90}$$

(the pre-factor $\beta\widetilde{\beta}$ can be found in eq. (B5) and the absorption coefficient α in eq. (B3)).

For example, for TAA solution with $c = 0.375$mM irradiated for 1-hour we get from eq. (90): $\sigma_0 P \approx 3.9$mW/cm at $P_0 = 22.2$mW. The corresponding convection velocity $v_z = v_0$ (defined in eq. (89)) is $v_z \approx 0.17\,$cm/s. The frequency of the oscillations, $\omega \equiv 2\pi/T_{\text{osc}}$, in the autocorrelation function $g^{(2)}(q, \tau)$ is defined in eq. (70) (note that $\underline{v}$ is directed vertically). Experimental data show that $T_{\text{osc}} \approx 5.5 \pm 0.2\,$ms for $30^0 < \theta < 150^0$ (cf. Fig. 9c) does not depend on the scattering angle θ. Using this T_{osc}, the theoretical v_z and eq. (70), we get the vertical tilt angle $\theta_z \sim 0.04 \approx 2^\circ$ which is a reasonable estimate (roughly in agreement with independent estimates of the tilt angle, cf. section 4.2) supporting the adopted assumption that the oscillations are defined by the thermo-convection velocity.

The theoretical dependence of the oscillation period $T_{\text{osc}} = 2\pi/\omega$ on the laser power P_0, obtained for $\theta_z = 0.035$ and $c = 0.375$mM using eqs. (70), (89), (90), is shown in Fig. 14a, where the experimental data (cf. Fig. 9d) are presented as well.

A similar comparison for the concentration dependence of $2\pi/\omega$ at $P_0 = 22$mW (cf. Fig. 9b) is shown in Fig. 14b. A good agreement is observed in both cases.

Turning to the temperature field, the typical laser-induced temperature increment in the layers above the laser beam (for $z_D < z \ll H$) can be obtained with eq. (82); for example, it gives $\Delta T_{mean} \simeq 0.5\, \widetilde{W}/R = 2\pi z_D T_b/R \approx 0.09$K for $c = 7.5$mM and $P_0 \approx 22$mW. By contrast, the local temperature rise in a narrow zone right above the beam with $z \sim z_D$, $y \lesssim \sqrt{z z_D}$, is much stronger (cf. eqs. (A13), (A2)): $\Delta T_{beam} \sim 0.24\sigma_0 P/(C_p D_T) \approx 3T_b$, so $\Delta T_{beam} \sim 5$K for the same c and P_0.

Let us finally verify the conditions (75) adopted above. The typical convection velocity is $v_z = v_0 \sim 0.1$cm/s (cf. eq. (89)). Hence $D_T/v_0 \sim 0.1$mm, and the first condition (75) is satisfied: $D_T/v_0 \sim d_{beam} \ll R = 2.5$mm. The second condition (75) is equivalent to $\nu \gg D_T$ (cf. eqs. (80), (81)), which simply follows from the chloroform material constants, eq. (74).

4.4. The nature of solute species providing the velocity contrast

The results of the previous section strongly support our hypothesis that oscillations of $g^{(2)}(q,\tau)$ must be related to the thermal convection flow $\underline{v}(\underline{r})$ induced by laser heating. However, as discussed in sections 3 and 4.2, the effect is also hinged on the existence of *two distinct* solute species moving with different velocities, $\underline{v}_1$ and $\underline{v}_2$, in irradiated TAA solutions.

Both microscopy and light-scattering data [9,12–14,18,20,30,36] suggest that most TAA molecules in irradiated solutions form fibrils of typical length $L \gtrsim 1\mu$m (in the studied concentration range of $0.3 - 10$mM). These micrometer-scaled self-assembling fibrils (together with shorter fibrils and other submicron aggregates) can be considered as the *first* component which must follow the macroscopic flow with velocity $\underline{v}_1 = \underline{v}(\underline{r})$ (recall that the characteristic size of convection flow, eq. (88), is much larger than the sizes of such aggregates).

Let us turn to the nature of the *second* component moving with a different velocity. The studies on chloroform TAA solutions [12–14,18,20,30,36] show that in addition to fibrils (of thickness $d \sim 5 - 15$nm) the solute molecules also form much longer fibrillar aggregates (bundles) of thickness $\sim 20 - 50$nm and almost indefinite length. Such fiber-like bundles can associate to produce highly viscous thermoreversible gels and entanglement networks. It is then possible to expect that a gel is formed below the beam (colder region), so that dangling chains from the gel can reach the laser beam region serving as the immobile component (with $v_2 = 0$). However, this explanation is not exactly consistent: the gel formation may be expected before the laser is switched on, and then the gel should lead to a dramatic increase of the solution viscosity which is not observed (the viscosity of TAA solutions is comparable to that of the solvent).

One may further argue, however, that a microgel (involving small gel particles) is formed instead of a continuous gel phase: in this case a strong viscosity increase may be avoided. However, if a large immobile gel particle of size $L_g \gg d_{beam}$ enters the scattering volume it would suppress convective flow there. On the other hand, if a microgel particle is smaller than the scattering volume size ($d_{beam} \sim 100\mu$m), it would be driven by the convection flow, so its velocity $\underline{v}_2$ would not differ much from $\underline{v}_1$.

To overcome this restriction let us consider a gel particle of size $r_p \lesssim d_{beam}$ and argue that it could be electrically trapped in the beam region. In fact, the particle is a network of TAA fibers which are known to be highly conductive after irradiation (with metallic-type conductivity) [14,18,20,30,36]. Hence the gel particles are expected to behave like metal particles in the laser beam if the network mesh size ξ is smaller than the laser wavelength λ. Using this analogy and assuming a spherical particle of radius r_p we get the trapping energy $U \simeq 0.5\, r_p^3 n^2 E^2$, where E is the effective electric field in the beam related to its intensity $I = nE^2 c_l/4\pi$ with c_l, the velocity of light in vacuum [37]. The effective laser power is $P \sim (\pi/4)\, I d_{beam}^2$. Thus

$$U \sim \frac{8n}{c_l} r_p^3 P/d_{beam}^2$$

The highest energy $U \sim P d_{beam}/c_l$ is attained for the largest particles with $r_p \sim d_{beam}/2$. For $P \sim 20$mW and $d_{beam} \sim 100\mu$m it becomes $U \sim 10^{-7}$erg. This energy is much larger than the thermal energy $k_B T$ (at ambient $T \approx 293$K): $U/k_B T \sim 2 \cdot 10^6$. Hence, the considered gel particle can be indeed strongly trapped by the laser beam under equilibrium conditions. However, in the presence of a convective flow the trapping is possible only if the laser-induced force $f_t \sim U/d_{beam}$ is stronger than the hydrodynamic drag force $f_d \sim 6\pi r_p \eta v_z$. For $r_p \sim d_{beam}/2$ and $v_z \sim 0.1$cm/s (as estimated in the previous section) this is not really the case:

$$f_t/f_d \sim U/\left(3\pi d_{beam}^2 \eta v_z\right) \sim 0.1$$

It is therefore not likely that the gel particles can be trapped in the laser beam for the range of laser powers ($P_0 \lesssim 20$mW) used in our DLS studies.

It is possible, however, that microgel particles involve very long dangling fibers. If the microgel is located well below the scattering volume, such giant fibers (with $L \gg d_{beam}$) could be dragged and extended by the convective flow (note that this flow is elongational near and below the laser beam, cf. Fig. 13). As a result a few thick and oriented fibers can stay basically immobile in the scattering volume (being anchored to the microgel) and therefore serve as the second scattering component with $\underline{v}_2 \approx 0$ (cf. Fig. 15). On the other hand, the convective flow of typical TAA fibrils (of $L \gtrsim 1\mu$m) should be effectively unperturbed if the distance between the giant fibers along the laser beam exceeds their length.

Yet another type of scattering species can be provided by gas bubbles of air dissolved in chloroform. The laser-induced heating of the sample can accelerate formation of these bubbles. Their nucleation should normally take place at the solid surfaces, so the bubbles must be dragged by the convective vortex motion to reach the scattering volume. This is possible only if the velocity $\underline{v}_b$ of their gravitational rising (always directed upwards and measured with respect to the local flux of the solution) is sufficiently low compared to the convective flow velocity $\underline{v}(\underline{r})$. In this case there would be two species in the scattering volume: TAA fibrils (moving with the flux velocity $\underline{v}_1 = \underline{v}(0,0) \simeq v_z \underline{n}_z$ which is directed upwards) and the bubbles (moving also upwards with the velocity $\underline{v}_2 = \underline{v}_1 + \underline{v}_b$), hence the $g^{(2)}$ oscillation eq. (67) would be defined by v_b: $\omega = q_z v_b$. In the peripheral part of the vortex convective motion (cf. eq. (88) for $|y| \gtrsim R/3$) the bubbles move downwards with velocity $|v_z| - v_b$, hence they follow the flow and can accumulate in time. The bubble rising velocity v_b depends on its radius r_b and can be found

by balancing the buoyancy force $f_b \approx \frac{4\pi}{3} r_b^3 \rho_0 g$ and the viscous drag force on an empty sphere $f_d \simeq 4\pi\eta r_b v_b$ [38]:

$$v_b \approx \frac{1}{3} r_b^2 \rho_0 g/\eta \tag{91}$$

(cf. also [39]). With $v_z \approx 0.1$cm/s (cf. section 4.3) the condition of the dominance of the convection flow over the buoyancy rising ($v_b < k v_z$ where $k < 1$ is a numerical factor) leads to

$$r_b < \sqrt{k} \cdot 10\mu\text{m}$$

cf. eq. (91). For $k \simeq 0.1$ this condition reads as $r_b < 3\mu$m, hence the respective bubbles are still large enough ($\gg \lambda_0/n$) and could give rise to a considerable scattering intensity comparable to the contribution of TAA fibrils. However, such large bubbles would be easily visible (with naked eye) as glittering particles. Such bubbles were not observed for the systems we studied, hence we tend to reject the bubble hypothesis and return to the model of microgels with dangling tails, Fig. 15.

5. Conclusions

In this paper we considered DLS data on dilute solutions of photosensitive arylamine-based compounds (TAA) in deuterated chloroform ($CDCl_3$). The solute molecules self-assemble forming long supramolecular fibrils and fibers upon white light exposure [12,13]. We show (by UV-Vis spectrometry) that the self-assembly is accompanied with a dramatic increase of the visible light absorbance of the studied TAA solutions [14]. This increase is found to be relatively slow, with time-scale ~ 5 min which is longer than the time required to convert nearly all TAA molecules in the aggregated state (few dozens of seconds [14]). However, the relevant time-scale should rather correspond to the growth time for the number of spins in the fibrils, which is much longer, typically ~ 1 hour [14]: the spins are known to be responsible for high electroconductivity of the fibrils. It is likely that the increase of light absorbance is related to the emerging high conductivity of supramolecular arylamine filaments which show metallic properties upon white light exposure [18,20,30,36]. It is important that high absorbance of irradiated TAA solutions in red part of visible spectrum was independently confirmed by direct measurements of transmitted laser beam intensity (see section 3).

Surprisingly, the photoinduced self-assembly also leads to a dramatic change of the DLS properties of the solutions showing long-lasting well-resolved oscillations in the intensity correlation function, $g^{(2)}(\tau)$, of the scattered laser light. Such feature is not expected for equilibrium Brownian systems which must always show a monotonically decaying correlation functions $g^{(2)}(\tau)$, cf. eq. (55). Thus, one of the main results of this paper is that self-assembly in solutions can be indicated by the emergence of oscillations in the DLS correlation function $g^{(2)}$. Moreover, we anticipate that the presence of such oscillations could be a sensitive probe for aggregation in many complex systems, including solutions of supramolecular and protein polymers, as well as conjugated and conducting macromolecules.

The oscillations we report here are strikingly well-developed and persistent, making our systems very distinct from the previously published oscillations in homodyne spectra $g^{(2)}$ of diverse light-absorbing systems, refs. [15,16,33,35]. We studied in detail how the oscillation frequency ω depends on various parameters. It is shown that ω regularly increases with the irradiation time t_{irr}, with TAA concentration c, and with the laser power P_0. Amazingly, we also observed that ω does not depend on the scattering angle θ (see Figs. 7, 9c), and this is the second major result of this study. It indicates that in our system the relevant processes (producing oscillations) have no horizontal velocity component, contrary to the systems of refs. [15,16].

There are only 2 general reasons to get oscillations in $g^{(2)}$: (i) due to inertial effects which are totally negligible at the wave-length of light for incompressible liquids like the studied solutions; (ii) due to non-equilibrium effects.

Focusing on the second possibility we showed that enhanced absorbance in TAA solutions leads to their non-uniform heating by the laser beam and to the thermal lensing effects due the emerging temperature (T) and refractive index (n) gradients (see section 3). In turn, a vertical gradient of n causes a small vertical downward shift of the incident laser beam (on the angle θ_z), while a significant increase of T near and above the scattering volume generates an upward convection flow in this region (see Figs. 4, 13). As a third major achievement, we developed a quantitative theory of this thermo-gravitational convection predicting the relevant vertical flow velocity v_0 as a function of the system parameters like the thermal expansion coefficient $\varkappa$ of the solution, and its absorption coefficient α which was obtained based on the transmitted laser intensity. The theory explains the observed independence of the oscillation frequency ω on the scattering angle θ. It also reproduces well (at the semi-quantitative level) the dependence of ω on the laser power P_0 and solution concentration c (see Fig. 14). The only fitting parameter θ_z was set to 2° which is in good agreement with the observed deflection of the laser beam.

Thus, based on the discussion in sections 4.2, 4.4 we showed that the observed oscillations in the DLS intensity correlation function $g^{(2)}(q,\tau)$ are related to thermo-gravitational convection generated by laser heating and leading to macroscopic drift of the scattering particles. It is also shown that the slow decay of the oscillations cannot be explained by a continuous variation of the particle drift velocity within the scattering volume. The oscillation effect points to the presence of two types of scattering particles in the solute moving with different velocities and a considerable velocity contrast $\Delta\underline{v} = \underline{v}_1 - \underline{v}_2$. As argued in section 2.4.c (and was proposed before [16]) the oscillation frequency ω must be proportional to Δv. We thus show that it is possible to determine the drift velocity difference by doing simple homodyne light scattering experiments. It appears that the order of magnitude of the oscillation frequency, $\omega \propto \Delta v$, and its dependencies on the parameters are correctly described by the assumption that Δv is simply proportional to the convection velocity v_z. One type of the scattering species can be attributed to micron-size supramolecular TAA fibrils. However, the nature of the second distinct scattering component is less evident. As a possible candidate we propose that this role is played by giant TAA fibers spanning from the scattering volume to a microgel particle.

Conflicts of interest

There is no conflicts of declare.

Acknowledgements

The authors acknowledge supports from LabEx CSC (the University of Strasbourg) and from the University Paris Diderot (the DLS setup)

APPENDIX A: Temperature field $\Delta T(y,z)$ in a smooth convection flow due to the heating by a narrow laser beam

Here we solve eq. (71) exactly for the case when the motion of the solvent is assumed to be homogeneous: $\underline{v} = \underline{v_0}$ and directed vertically upwards. To simplify the treatment we also assume that a very narrow beam is switched-on at $t = 0$:

$$I(\underline{r}, t) = \begin{cases} P\delta(\underline{r}), & t \geq 0; \\ 0, & t < 0 \end{cases} \tag{A1}$$

where $\delta(\underline{r}) = \delta(y)\delta(z)$ is the 2-dimensional delta-function, cf. eq. (79). The temperature field $\Delta T(y, z, t)$ is hence essentially two-dimensional in space.

We first discuss the short-time asymptotic solution of eq. (71). The thermal diffusion is fast compared to the drift v_0 in the region close to the beam, $z^2 + y^2 \ll z_D^2$, cf. eq. (80). Omitting the convection term $\underline{v} \cdot \nabla T$ we solve the diffusion equation (71) (which becomes decoupled from the velocity field) to get the time-dependent temperature field $T(\underline{r}, t)$ after switching-on the laser beam at $t = 0$. The result for the temperature field at $t > 0$ (obtained on assuming that $\Delta T \equiv 0$ for $t < 0$ which means no heating without laser beam) is

$$\Delta T(\underline{r}, t) = \frac{\sigma_0 P}{C_p} \int_0^t \frac{1}{4\pi D_T t} \exp(-\frac{r^2}{4D_T t}) \mathrm{d}t = T_b E_1 \left(\frac{r^2}{4D_T t} \right), \qquad T_b \equiv \frac{\sigma_0 P}{4\pi D_T C_p} \tag{A2}$$

where

$$E_1(x) \equiv \int_x^\infty \left[\mathrm{e}^{-t}/t \right] \mathrm{d}t \tag{A3}$$

is the integral exponential function. For small x:

$$E_1(x) \simeq -\gamma - \ln x + \sum_{k=1}^{\infty} \frac{(-1)^{k+1} x^k}{k \cdot k!} \tag{A4}$$

$\gamma \simeq 0.577$ is the Euler-Mascheroni constant, $E_1(1) \simeq 0.22$ and $E_1(x) \simeq \mathrm{e}^{-x}/x$ for $x \gg 1$. For fixed distance r from the beam, the temperature rise can be approximated as

$$\Delta T(\underline{r}, t) \simeq T_b \times \begin{cases} (t/t_D(r))\, \mathrm{e}^{-t_D(r)/t}, & t \ll t_D \equiv r^2/4D_T; \\ \ln(t/t_D(r)) - \gamma, & t_D \ll t \ll \tau_D = D_T/v_0^2 \end{cases} \tag{A5}$$

if $r \ll z_D$ (the latter condition is needed for the inequality $t_D \ll \tau_D$). The conditions $r \ll z_D$ and $t \ll \tau_D \equiv z_D/v_0$ and are needed to neglect the convection term $\underline{v_0} \cdot \nabla T$ in eq. (71).

After switching-on the laser beam, ΔT is first exponentially low (for $t \ll t_D$), then it grows logarithmically up to the maximum

$$\Delta T^*(r) \simeq T_b \ln(\tau_D/t_D) \simeq 2T_b \ln(z_D/r) \tag{A6}$$

at $t \sim \tau_D$, cf.eq. (A5). At longer times $t \gtrsim \tau_D$: ΔT saturates due to the convection (drift v_0) providing a flux of fresh cold liquid from the lower part of the solution (with $z < -z_D$) where $T \approx T_{out}$, see Fig. 13.

The general solution of eq. (71) with $\underline{v} = v_0 \underline{n}_z$ and localized beam, eq. (A1), can be written for $t > 0$ using Green functions (cf. eq. (A2)):

$$\Delta T(y,z,t) = T_b \int_0^t \exp\left(-\frac{(z - v_0 t')^2 + y^2}{4D_T t'}\right) \frac{\mathrm{d}t'}{t'} =$$

$$= T_b \exp\left(\frac{v_0 z}{2D_T}\right) \int_0^{v_0 t/r} \exp\left(-\frac{v_0 r}{4D_T}\left[\tau + \frac{1}{\tau}\right]\right) \frac{\mathrm{d}\tau}{\tau} \tag{A7}$$

where $\tau \equiv t' v_0/r$, $r \equiv \sqrt{y^2 + z^2}$. Here we assumed (as before) that the laser beam was turned on at $t = 0$, so $\Delta T \equiv 0$ for $t < 0$. The above equation for ΔT (like eq. (A2)) is valid for $r \gg d_{beam}$.

Let us now focus on the steady regime, $v_0 t/r \to \infty$, when the convection flow is fully developed. Setting the upper limit in the integral (A7) to $+\infty$, we get for $t \gg \tau_D$ (cf. eq. (80)):

$$\Delta T(y,z) \simeq 2T_b \exp\left(\frac{z}{2z_D}\right) K_0\left(\frac{r}{2z_D}\right) \tag{A8}$$

where K_0 is a modified Bessel function, $K_0(x) = \int_0^\infty \exp(-x\cosh\tau)\mathrm{d}\tau$; $K_0(x) \simeq \ln(2/x) - \gamma$, $z \ll 1$; $K_0(x) \simeq \sqrt{\pi/(2x)}e^{-x}$, $x \gg 1$. For $z \gg z_D$ eq. (A8) can be simplified as

$$\Delta T(y,z) \simeq 2T_b \sqrt{\frac{\pi z_D}{z}} \exp\left(-\frac{y^2}{4 z z_D}\right) \tag{A9}$$

which coincides with eq. (77). At shorter distances $d_{beam} \ll r \ll z_D$, the asymptotic result is

$$\Delta T \simeq 2T_b \left[\ln\frac{4z_D}{r} - \gamma\right] \tag{A10}$$

The above equation agrees with the more approximate eq. (A6). Finally, below the beam, at $z < 0$, $|z| \gg z_D$ we obtain from eq. (A8):

$$\Delta T(y,z) \simeq 2T_b \sqrt{\frac{\pi z_D}{|z|}} \exp\left(-\frac{y^2}{4 z z_D}\right) \exp\left(-\frac{|z|}{z_D}\right) \tag{A11}$$

Hence, the temperature increment is exponentially small, so $T \approx T_{out}$ in this region below the beam.

The temperature profile right above the beam, at $y = 0$, $z \gg d_{beam}$, is

$$\Delta T(z) \simeq 2T_b \exp\left(\frac{z}{2z_D}\right) K_0\left(\frac{z}{2z_D}\right) \tag{A12}$$

In particular,

$$\Delta T(z_D) \simeq 3.048 T_b \approx 0.24 \frac{\sigma_0 P}{D_T C_p} \tag{A13}$$

APPENDIX B: Evaluation of the light absorption rate $\sigma_0 P$ causing the convection

The convection velocity v_0 in the scattering volume (within the sample illuminated by a focused laser beam) is defined in eq. (89). Apart from the material constants of chloroform, cf. eqs. (73), (74), v_0 depends on the absorption coefficient σ_0 and the local laser power P. Here we evaluate them based on our experimental data, Table 1.

To this end we first note that pure solvent (chloroform) nearly does not absorb visible light, so σ_0 must be entirely due to the solute (TAA). A linear dependence of σ_0 on c is naturally expected at low concentrations c:

$$\sigma_0 = \alpha c \tag{B1}$$

Hence the expected transmitted laser power P_2 after the sample in a DLS experiment (cf. Fig. 2) is proportional to the incident laser power P_0 and the exponential decay factor:

$$P_2 = \beta_{02} P_0 \exp(-2\alpha c R) \tag{B2}$$

where $R = 2.5$mm is the inner radius of the test tube and β_{02} is the instrumental coefficient accounting for the power loss outside the sample (due to interface reflections, diaphragms, etc.). β_{02} can be defined as $\beta_{02} = P_2^{(0)}/P_0 \approx 0.72 \pm 0.025$, where $P_2^{(0)}$ is the transmitted laser power for the case when instead of the sample a test tube with pure solvent ($c = 0$) is used (see second line in Table 1).

The absorption coefficient α depends on the irradiation pre-history of a TAA solution (i.e., on t_{irr} and t_{inc}, cf. Fig. 1d and Table 1). To find α for solutions irradiated during $t_{irr} = 1$ hour (with $t_{inc} = 0$) we compare the transmitted laser power P_2 after the sample for pure solvent and for TAA solutions of several concentrations c (using the maximum incident laser power $P_0 \simeq 21 - 22$mM to reduce the experimental error). Thus, for $c = 0.375$mM from Table 1 we get $\beta_{02} P_0/P_2 \simeq 1.09 - 1.25$, whereas for $c = 7.5$mM this ratio is $\beta_{02} P_0/P_2 \simeq 8.2 - 9.25$. Using the data for $c = 7.5$mM and the relation (B2) we find the absorption coefficient:

$$\alpha = [2Rc]^{-1} \ln\left[\beta_{02} P_0/P_2(c)\right] \approx 0.58 \pm 0.05\,(\mathrm{cm \cdot mM})^{-1} \tag{B3}$$

for $t_{irr} = 1$ hour and $t_{inc} = 0$. For longer incubation time t_{inc} the absorption coefficient decreases: $\alpha \approx 0.5 \pm 0.05$ $(\mathrm{cm \cdot mM})^{-1}$ for $t_{inc} = 1$h and $\alpha \approx 0.125 \pm 0.015$ $(\mathrm{cm \cdot mM})^{-1}$ for $t_{inc} = 19$h.

We now recall that the effective power P corresponds to laser intensity in the scattering volume located near the the center of the sample. The laser beam power P_1 just before entering the decaline bath (cf. Fig. 2) is lower than P_0; our measurements give $P_1 = \beta P_0$, where the factor $\beta \approx 0.88$ accounts for the power loss due to reflections caused by lens L1 and its aperture. Next, $P_1' = \widetilde{\beta} P_1$ is the laser power at the beginning of the passway inside the TAA solution bath. The coefficient $\widetilde{\beta}$ was calculated using the Fresnel formula for the reflection coefficient $R = R(i,j)$ at an interface between two media (i) and (j):

$$R(i,j) = \frac{(n_i - n_j)^2}{(n_i + n_j)^2} \tag{B4}$$

where n_i is refractive index of medium i. The transmission coefficient $K(i,j) = 1 - R(i,j)$, so the total coefficient of transmission through the air-glass-decaline-glass-chloroform sequence of interfaces is:

$$\widetilde{\beta} = \prod_{i=0}^{3} K(i, i+1) \simeq 0.965, \qquad \beta\widetilde{\beta} \simeq 0.85 \tag{B5}$$

where $n_0 = 1$ (air), $n_1 = n_3 = 1.4585$ (quartz), $n_2 = 1.481$ (decaline), $n_4 = 1.4458$ (chloroform). An additional laser absorption in TAA solution (from the point of entering till the center of the test tube) leads to $P \simeq P_1' \exp(-\alpha c R) = P_0 \beta \widetilde{\beta} \exp(-\alpha c R)$. Finally, we get the light energy absorption rate in the scattering volume

$$\sigma_0 P \simeq \beta \widetilde{\beta} \alpha c P_0 \exp(-\alpha c R) \tag{B6}$$

References

[1] B. J. Berne, R. Pecora. Dynamic Light Scattering With Applications to Chemistry, Biology, and Physics (Dover Publications INC., Mineola, New York, 2000).

[2] C. S. Johnson, Jr., D. A. Gabriel. Laser Light Scattering (Dover Publications INC., New York, 1994).

[3] W. Schärtl. Light Scattering from Polymer Solutions and Nanoparticle Dispersions (Springer, New York, 2007).

[4] Photon Correlation and Light Beating Spectroscopy, ed. H. Cummins, Nato Science Series B Vol. 3 (Springer, New York, 1974).

[5] B. Chu. Laser Light Scattering, Basic Principles and Practice (Dover Publications INC., Mineola, New York, 2007).

[6] N. Jouault, Y. J. Xiang, E. Moulin, G. Fuks, N. Giuseppone, and E. Buhler, Phys. Chem. Chem. Phys. 2012, v.14, 5718.

[7] J. Appell, G. Porte, and E. Buhler, J. Phys. Chem. B 2005, v.109, 13186.

[8] E. Buhler, J. P. Munch, and S. J. Candau, Europhys. Lett. 1996, v.34, 251.

[9] N. Jouault, E. Moulin, N. Giuseppone, E. Buhler, Phys. Rev. Lett. 2015, v.115, 085501.

[10] L. Brunsveld, B. Folmer, E. Meijer, R. Sijbesma, Chem. Rev. 2001, v.101, 4071.

[11] J.-M. Lehn, Angew. Chem. Int. Ed. 2013, v.52, 2836.

[12] E. Moulin, F. Niess, M. Maaloum, E. Buhler, I. Nyrkova, and N. Giuseppone, Angew. Chem., Int. Ed. 2010, v.49, 6974.

[13] E. Moulin, J. J. Armao IV, N. Giuseppone, Acc. Chem. Res. 2019, v.52, 975-983.

[14] I. Nyrkova, E. Moulin, J. J. Armao IV, M. Maaloum, B. Heinrich, M. Rawiso, F. Niess, J.-J Cid, N. Jouault, E. Buhler, A. N. Semenov, N. Giuseppone, ACS Nano 2014, v.8, 10111-10124.

[15] W. Schaertl, C. Roos, Phys. Rev. E 1999, v.60, 2020-2028.

[16] A. Sehgal, T. A. P. Seery, Macromolecules 1999, v.32, 7807-7814.

[17] W. Schaertl, C. Roos, K. Gohr, J. Chem. Phys. 1998, v.108, 9594.

[18] V. Faramarzi, F. Niess, E. Moulin, M. Maaloum, J. F. Dayen, J. B. Beaufrand, S. Zanettini, B. Doudin, and N. Giuseppone, Nat. Chem. 2012, v.4, 485.

[19] E. Moulin, J. J. Cid, and N. Giuseppone, Adv. Mater. 2013, v.25, 477.

[20] J. J. Armao, M. Maaloum, T. Ellis, G. Fuks, M. Rawiso, E. Moulin, and N. Giuseppone, J. Am. Chem. Soc. 2014, v.136, 11382.

[21] Y. Domoto, E. Busseron, M. Maaloum, E. Moulin, and N. Giuseppone, Chem. Eur. J. 2015, v.21, 1938.

[22] E. Busseron, J.-J. Cid, A. Wolf, G. Du, E. Moulin, G. Fuks, M. Maaloum, P. Polavarapu, A. Ruff, A.-K. Saur, S. Ludwigs, and N. Giuseppone, ACS Nano 2015, v.9, 2760.

[23] E.R.Pike. Photon Correlation Velocimetry. In: "Photon Correlation Spectroscopy and Velocimetry" edited by H.Z.Cummins, E.R.Pike (Plenum, New York, 1977).

[24] N. Ben-Yosef, S. Zeigenbaum, A. Weitz, Appl. Phys. Lett. 1972, v.21, 436.

[25] R. V. Mustacich, B. R. Ware, Phys. Rev. Lett. 1974, v.33, 617.

[26] T. Tanaka, G. B. Benedek, Applied Optics 1975, v.14, 189-196.

[27] B.R.Ware, W.H.Flygare, Chem. Phys. Lett. 1971, v.12, 81.

[28] B.R.Ware, W.H.Flygare, J. Coll. Int. Sci. 1972, v.39, 670.

[29] A.Wada, I.Nishio, K.Soda, Rev. Sci. Instrum. 1979, v.50, 458.
[30] J. J. Armao IV, I. Nyrkova, G. Fuks, A. Osypenko, M. Maaloum, E. Moulin, R. Arenal, O. Gavat, A. Semenov, and N. Giuseppone, J. Am. Chem. Soc., 2017, v.139, 2345-2350.
[31] S.W. Provencher. "CONTIN: A general purpose constrained regularization program for inverting noisy linear algebraic and integral equations". Computer Physics Communications, 1982, v.27, 229-242. doi:10.1016/0010-4655(82)90174-6.
[32] S.W.Provencher. "A constrained regularization method for inverting data represented by linear algebraic or integral equations". Computer Physics Communications 1982, v.27, 213-227. doi:10.1016/0010-4655(82)90173-4
[33] G. G. Fuller, J. M. Rallison, R. L. Schmidt, L. G. Leal, J. Fluid Mech. 1980, v.100, 555-575.
[34] N. V. Tabiryan, W. Luo, Phys. Rev. E 1998, v.57, p.4431.
[35] R. S. Hall, Y. S. Oh, C. S. Johnson, Jr., J. Phys. Chem. 1980, v.84, 756-767.
[36] J. J. Armao IV, P. Rabu, E. Moulin, N. Giuseppone, Nano Lett. 2016, v.16, 2800-2805.
[37] L.D.Landau and E.M.Lifshitz. Electrodynamics of Continuous Media (Volume 8 of A Course of Theoretical Physics). (Pergamon Press, 1960).
[38] D.J. Acheson, Elementary Fluid Dynamics. (Clarendon Press, Oxford, 2005).
[39] L. Parkinson, R. Sedev, D. Fornasiero, J. Ralston, Journal of Colloid and Interface Science, 2008, v.322, 168-172.

TABLES

TABLE 1. The main DLS characteristics of the studied samples: the reference solvents (toluene, $CDCl_3$) and the TAA solutions in chloroform ($CDCl_3$). The main preparation parameters of the TAA samples (concentration, irradiation time t_{irr}, incubation time in the dark after irradiation, t_{inc}) are indicated together with the incident laser light power P_0, the transmitted laser power P_2, the intensity of the scattered light, $I_3^{\rm exp}$ (measured by the APD at $\theta = 90^0$), and the corrected net sample scattering intensity without the dark noise, I_3 [7], and the oscillation period $T_{\rm osc}$ of $g^{(2)}(\tau)$. The ratios $P_2/P_2^{\rm tol}$ and $I_3/I_3^{\rm tol}$ are also shown ($P_2^{\rm tol}$ and $I_3^{\rm tol}$ are the reference values measured for pure toluene and the same laser intensity P_0). The error bars are: $\simeq 0.03 - 0.05$mW for P_0; $\simeq 7\% + 0.1$mW for P_2; $\simeq 0.5$kHz for I_3, and $\simeq 1\%$ for $T_{\rm osc}$.

TABLE 2. Parameters of the theoretical fits based on eq. (56) for the DLS data on the intensity correlation functions $g^{(2)}(\tau) - 1$ shown in Figures 3, 8. The columns indicate Figure numbers, curve labels, initial (short-time) decay parameters τ_i and G_i, oscillation parameters $T_{\rm osc}$, $\tau_{\rm osc}$ and $G_{\rm osc}$, and terminal decay parameters τ_e and G_e.

FIGURE CAPTIONS

FIG. 1. (color online) (a) Chemical structure of the tailored triarylamine (TAA) molecule (chemical formula $C_{36}H_{49}ClN_2O_3$, molecular weight of 593.25 g/mol) used in our experiments (upper left); schematic representation of the supramolecular self-assembling micrometric conducting nanowires formed by the amine molecules upon light irradiation. Molecular models of TAA unimer (b), and of the double fibril (front and side views) (c) which are the basic elements of the TAA self-assembling nano-wires. (d) UV-Vis absorption spectra of a 1mM freshly-prepared TAA solution in chloroform before irradiation ($t_{irr} = 0$ s, black line), after a period, $t_{irr} = 765$ s, of irradiation with 20W glow-filament white lamp (blue line), after $t_{irr} = 3765$ s (green line) and after both irradiation (for $t_{irr} = 3765$ s) and incubation in the dark for $t_{inc} = 14400$ s (dashed grey line). The inset shows the time evolution of the absorbance at $\lambda = 635$ nm for the first TAA solution during the irradiation stage (0-3765s) and the dark stage (3750-18165s); the dashed line is a guide to the eye.

FIG. 2. The schematic DLS set-up. The lens L1 focuses the incident beam (with wavevector $\mathbf{k}_1$) onto the test tube with a sample solution (TS) placed into the thermostated decaline bath (DB). The lenses L2 and L3 focus the light (with wavevector $\mathbf{k}_2$) scattered from the scattering volume (SV) onto the photodetector

---

[7] The experimental APD data, $I_3^{\rm exp}$, have been corrected as $I_3 \equiv I_3^{\rm exp} - I_3^{\rm dark}$, where $I_3^{\rm dark} \simeq 1.45 \pm 0.12$ kHz is the 'dark noise level intensity' measured on the detector when the laser is shut off and the sample is out of the decaline bath ($I_3^{\rm dark}$ comes from the parasitic light, thermal noise on the detector, etc.).

(PD). The scattering vector is $\mathbf{q} = \mathbf{k_2} - \mathbf{k_1}$ (the scattering angle is θ). The focal lengths of the lenses are respectively: $F_1 = F_2 = 250$mm and $F_3 = 3.9$mm. The characteristic distances shown on the scheme are: $x_1 = x_2 = 250$mm, $x_3 = 125$mm. The intensity of laser light was measured at the laser exit (incident power P_0 at point '0'), before entrance in the sample, at point '1' (laser beam intensity P_1) and after the sample, at the point '2' (P_2, the transmitted intensity) using the same type of the power meter. The scattering intensity I_3 and the intensity autocorrelation function $G^{(2)}(q,\tau)$, eq. (7), were measured by the photodetector PD at the point '3'. The intensities at the point '1'' inside the test tube ($P_1' = \widetilde{\beta} P_1$) and at the point '$*$' near the SV ($P = \widetilde{\beta} P_1 \exp(-\alpha c R)$) were calculated as described above eq. (90).

FIG. 3. Intensity correlation functions measured in the homodyne DLS (averaging time $t_{DLS} = 1$ hour, scattering angle $\theta = 90^0$) for c =7.5mM (0.45 vol%) TAA chloroform solutions irradiated with short white pulses prior to the measurement. [8] (a) The traditional log-log plot of time-dependence of autocorrelation functions $g^{(2)}(q,\tau) - 1$ for three irradiation times (t_{irr} =5, 10, and 15s). (b) Semi-log plot of the same autocorrelation functions. Black crosses show the DLS data (with incident laser power P_0 =22.2 mW). Red curves represent the theoretical fits using eq. (56). The curves are shifted vertically to improve the visibility.

FIG. 4. A scheme illustrating an expansion of the incident laser beam (due to the thermal lensing effect) and its vertical shift (due to the vertical temperature gradient near the beam coming from strong light absorption in TAA solutions). The photograph (right) shows the diffraction rings pattern in the transmitted beam observed on a screen at a distance L =160cm from the scattering sample. Here the incident light wave-vector, $\mathbf{k_0}$, does not coincide with the wave-vector $\mathbf{k_1}$ of the transmitted light: $\mathbf{k_1} = \mathbf{k_0} - \mathbf{q}_z$. The scattered light wave-vector, $\mathbf{k_2}$, is perfectly horizontal (like $\mathbf{k_0}$), but the effective scattering vector $\mathbf{q} = \mathbf{k_2} - \mathbf{k_1}$ is not: it involves a vertical component $q_z \sim \theta_z k$, where $\theta_z = \Delta z / L$.

FIG. 5. Intensity autocorrelation function, $g^{(2)}(\tau) - 1$, averaged over $t_{DLS} = 200$s for a TAA solution with $c = 7.5$mM and various incubation times t_{inc} in the dark after it was irradiated for (a) $t_{irr} = 5$s and (b) $t_{irr} = 1$h. The data are recorded for the scattering angle $\theta = 90^0$ and laser power P_0 =22.2mW. The curves are shifted vertically to improve the visibility.

FIG. 6. TAA concentration dependence of the intensity correlation function, $g^{(2)}(\tau) - 1$ (averaged over $t_{DLS} = 200$s, recorded at $\theta = 90^0$ and $P_0 = 22.2$ mW). All solutions were illuminated for $t_{irr} = 1$h prior to the measurements ($t_{inc} = 0$). The curves are shifted vertically to improve the visibility.

FIG. 7. Angular dependence of the intensity correlation function: $g^{(2)}(\tau) - 1$ was recorded at various scattering angles, θ, for $c = 0.375$mM TAA solution irradiated

---

[8] For irradiation of TAA samples we routinely use a 20W white glow-filament lamp placed at a distance of 5cm from the sample. This procedure is the same as used in our previous works on TAA self-assembly, refs. [12,14].

for $t_{irr} = 1$h and left at rest in the dark for $t_{inc} = 3$h30min. The incident laser power is $P_0 = 22.2$mW; $t_{DLS} \sim 200$s for $\theta = 90^0 - 140^0$, $t_{DLS} \sim 60$s for $\theta = 70^0 - 80^0$, and $t_{DLS} \sim 20$s for $\theta = 30^0 - 60^0$. The dashed line shows the θ-independent position of the first oscillation. The curves are shifted vertically to improve the visibility.

FIG. 8. Variation of the intensity correlation function with the incident laser power P_0 for 0.375mM TAA solution irradiated for $t_{irr} = 1$hour and left at rest in the dark for $t_{inc} \simeq 5$h15min-5h35min . The function $g^{(2)}(\tau)$ was measured at $\theta = 90^0$, the DLS-averaging time was $t_{DLS} = 200$s. The log-log plots of $g^{(2)}(q,\tau) - 1$ are shifted vertically to improve the visibility. The data (black crosses) are fitted using eq. (56) (the respective red curves), see Table 2 for the fitting parameters.

FIG. 9. The period of oscillations, $T_{\rm osc} = 2\pi/\omega$ (circles), and the associated effective drift speed v^*, eq. (66) (triangles), are plotted as functions of: (a) irradiation time t_{irr} (for 7.5mM TAA solution); (b) TAA concentration c (for solutions irradiated for $t_{irr} = 1$ hour); (c) scattering vector q (for solution of $c = 0.375$mM irradiated for $t_{irr} = 1$ hour and incubated for $t_{inc} \simeq 3.5 - 4$h); and (d) incident laser power P_0 (for solution of $c = 0.375$mM irradiated for $t_{irr} = 1$ hour). In (a-c) the incident laser power is $P_0 = 22.2$mW, in (a,b,d) the scattering angle is $\theta = 90^0$. The dashed lines are guides to the eye.

FIG. 10. Intensity correlation function from two aged self-assembled TAA solutions with $c = 0.375$mM (a) and $c = 7.5$mM (b) obtained during their sonication in the dark for 2h (after their irradiation for $t_{irr} = 1$h and incubation for $t_{inc} = 42$h). The functions $g^{(2)}(\tau)$ were recorded every 30mins during the sonication, and finally at $t_{rest} = 3$h after the end of 2h sonication. The DLS averaging time was $t_{DLS} = 20$s for all measurements apart from the last measurement (for $t_{rest} = 3$h) where $t_{DLS} = 200$s. The curves are shifted vertically to improve the visibility.

FIG. 11. Intensity correlation function of a freshly prepared TAA solution of $c = 0.375$mM which was simultaneously sonicated and irradiated with white light during 1 hour. The data were recorded every 10 mins. $t_{DLS} = 10$s was chosen to be very short so that the sonication/illumination process was only briefly interrupted, explaining the higher noise level. The curves are shifted vertically to improve the visibility.

FIG. 12. (a) Fittings of the experimental auto-correlation function $g^{(2)}(\tau)$ (from Fig. 3b, for $t_{irr} = 5$s) with the 'oscillatory relaxation model' (implying two distinct drift speeds v_1 and v_2), eq. (56) (red line), and with the 'velocity gradient model' for the slit geometry, eq. (65) (black line). (b) The three classical diffraction 'smearing functions': $\widetilde{g}_1$ ('slit', black line), $\widetilde{g}_2$ ('cylindrical', blue line) and $\widetilde{g}_3$ ('spherical', green line), eqs. (62), (63), (64), respectively. All fitting and smearing functions are shown for the same period $T_{\rm osc} \equiv 2\pi/\omega = 7 \times 10^{-3}$s used for theoretical fits with eq. (56).

FIG. 13. Convection flow in the slit $-R \leq y \leq R$ filled with light-absorbing viscous liquid (a), the heated zone above the laser beam (b) and the temperature profile $\Delta T(z) \equiv T(z) - T_{out}$ in the center of the slit, for $y = 0$ (c). The beam of diameter d_{beam} directed along the x-axis is shown with red/yellow star. The

cross-over distance $z_D \equiv D_T/v_0$ separates the proximal zone (where the diffusion is more important than the drift) and the far zone (where the heat propagation is dominated by the drift).

FIG. 14. The oscillation period $T_{\rm osc}$ of $g^{(2)}(\tau)$ as a function of: (a) the incident laser power P_0 (for TAA solution with $c = 0.375$mM), and (b) the TAA concentration c (for $P_0 = 22.2$ mW). All solutions were irradiated for $t_{irr} = 1$hour ($t_{inc} = 0$) prior to the measurements of $g^{(2)}(\tau)$, the scattering angle was $\theta = 90^0$. The solid curves are theoretical predictions obtained using eqs. (70), (89) with $v_z = v_0$ and $\theta_z = 0.035 \approx 2^\circ$.

FIG. 15. On the origin of two distinct velocities in the scattering volume: small fibrils move through the beam with the convective flow velocity $v_1 = v_0$ while long fibers are anchored to microgel particles with $v_2 \approx 0$.

Table 1.

Sample	t_{irr}	t_{inc}	P_0 (mW)	P_2 (mW)	P_2/P_2^{tol}	I_3^{exp} (kHz)	I_3 (kHz)	I_3/I_3^{tol}	T_{osc} (ms)
Toluene	-	-	22.2	16.1	1	27.83	26.4	1	-
$CDCl_3$	-	-	22.2	16.0	0.99	16.06	14.61	0.55	-
Decalin bath without test tube	-	-	21.6	15.8	1.01	10.51	9.06	0.35	-
TAA 7.5mM	0	-	22.2	14.9	0.93	21.98	20.53	0.78	-
TAA 7.5mM	5s	0 min	22.2	14.7	0.91	22.55	21.10	0.80	7.1
		10 min	22.2	14.9	0.93	22.27	20.82	0.79	7.6
		30 min	22.2	14.0	0.87	22.90	21.45	0.81	6.9
		1 hour	22.2	14.7	0.91	22.24	20.79	0.79	7.6
		2 hours	22.2	14.2	0.88	19.69	18.24	0.69	8.3
		3 hours	22.2	14.2	0.88	19.73	18.28	0.69	6.8
		4 hours	22.2	14.9	0.93	19.69	18.24	0.69	6.7
		19 hours	21.2	12.6	0.82	19.16	17.71	0.70	8.5
TAA 7.5mM	1 hour	0 min	22.2	1.86	0.12	3.54	2.09	0.08	2.7
		10 min	22.2	2.10	0.13	3.94	2.49	0.09	2.4
		30 min	22.2	2.17	0.13	4.14	2.69	0.10	2.5
		1 hour	22.2	2.42	0.15	4.42	2.97	0.11	2.3
		2 hours	22.2	3.53	0.22	5.39	3.94	0.15	2.6
		3 hours	22.2	4.38	0.27	6.19	4.74	0.18	2.5
		19 hours	21.2	9.22	0.60	12.67	11.22	0.44	3.5
		42 hours	22.2	-	-	13.98	12.53	0.47	3.8
TAA 0.375mM	1 hour	0 min	21.2	13.13	0.82	13.25	11.80	0.45	6.4
		1 hour	22.2	13.2	0.82	15.76	14.31	0.54	5.4
		2 hours	22.2	13.8	0.86	14.51	13.06	0.49	5.7
		3 hours	22.2	13.6	0.84	15.15	13.70	0.52	5.7
		19 hours	21.2	14.6	0.95	14.83	13.38	0.53	8.0
		42 hours	22.2	-	-	14.3	12.85	0.49	9.0
TAA 0.375mM	1 hour	5h15min	22.0	14.7	0.92	17.12	15.67	0.60	6.0
		5h20min	12.0	8.25	0.95	9.42	7.97	0.56	8.0
		5h25min	5.0	2.75	0.76	4.67	3.22	0.54	12.3
		5h30min	2.5	1.47	0.81	2.70	1.25	0.49	24
		5h35min	1.0	0.50	0.69	1.77	0.32	0.42	42
TAA 3.75mM	1 hour	0 min	22.2	-	-	6.6	5.15	0.20	3.7
TAA 0.75mM	1 hour	0 min	22.2	-	-	9.4	7.95	0.30	5.6

Table 2.

Figure	Curve	τ_i (s)	G_i	T_{osc}(s)	τ_{ocs} (s)	G_{osc}	τ_e (s)	G_e
Fig.3	5s	5×10^{-8}	23	0.0070	0.027	0.0095	0.12	0.025
		2.5×10^{-7}	0.70					
		2×10^{-6}	0.05					
		3.5×10^{-5}	0.03					
		7×10^{-4}	0.003					
	10s	5×10^{-8}	15	0.0075	0.033	0.90	0.27	4.15
		1.7×10^{-7}	2.0					
	15s	5×10^{-8}	15	0.0058	0.015	1.8	0.15	10
		1.2×10^{-7}	3.0					
Fig.8	22.2mW	5×10^{-7}	0.4	0.0060	0.025	0.065	0.13	0.25
		5×10^{-4}	0.07					
	12mW	3×10^{-7}	0.9	0.0080	0.02	0.03	0.1	0.07
		5×10^{-6}	0.07					
		3.5×10^{-4}	0.03					
	5mW	1.5×10^{-6}	0.3	0.0123	0.05	0.04	0.25	0.1
		4×10^{-5}	0.1					
		3×10^{-3}	0.05					
	2.5mW	2×10^{-6}	0.5	0.024	0.1	0.01	0.22	0.025
		6×10^{-5}	0.15					
		1.5×10^{-3}	0.02					
	1mW	5×10^{-6}	0.7	0.042	0.3	0.025	1.0	0.15
		1×10^{-4}	0.17					
		2×10^{-2}	0.06					

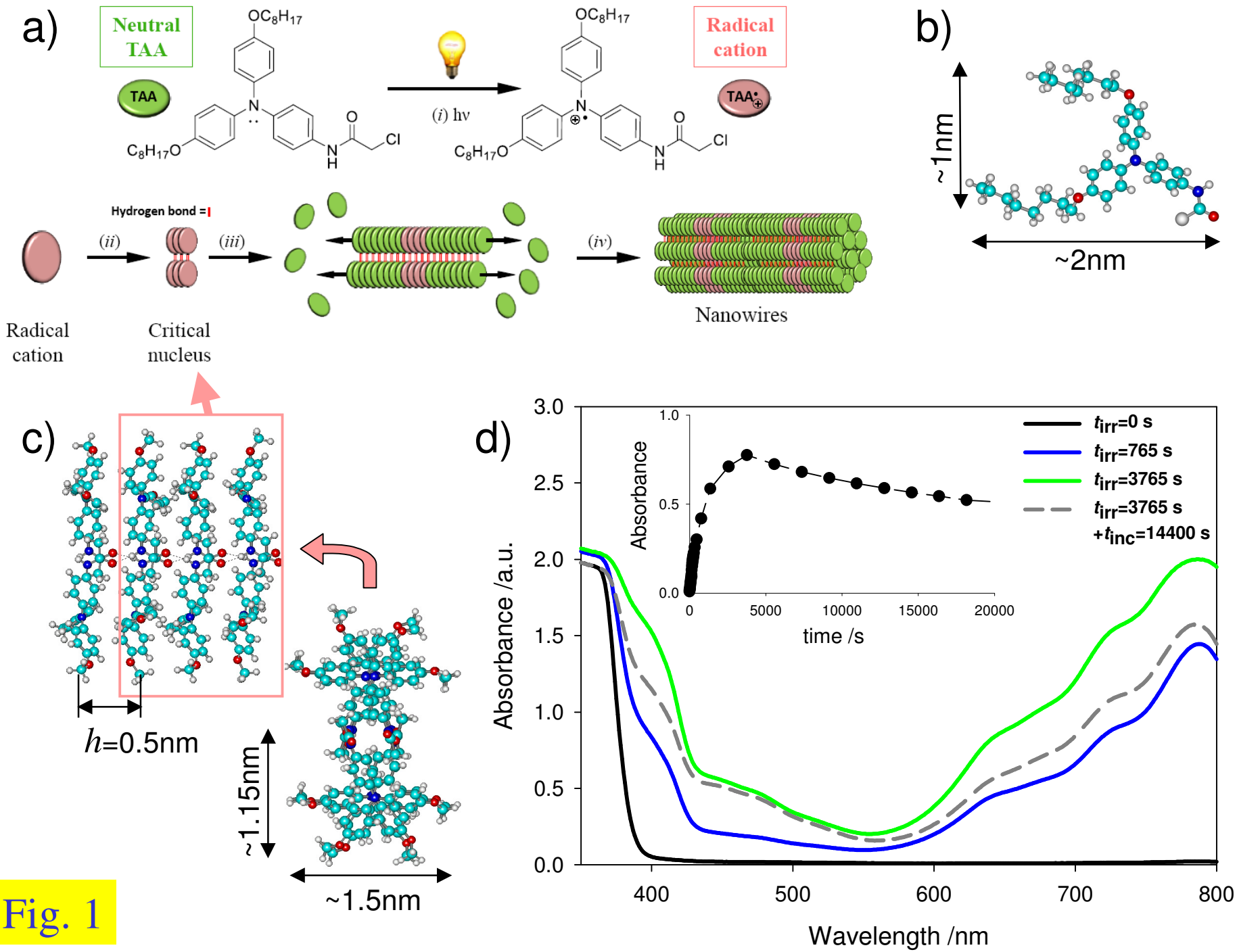
a)
Neutral TAA
TAA
Radical cation
TAA•⊕
(i) hν
Hydrogen bond
(ii)
(iii)
(iv)
Radical cation
Critical nucleus
Nanowires
b)
~1nm
~2nm
c)
h=0.5nm
~1.15nm
~1.5nm
d)
Absorbance /a.u.
Wavelength /nm
Absorbance
time /s
t_irr=0 s
t_irr=765 s
t_irr=3765 s
t_irr=3765 s +t_inc=14400 s

Fig. 1

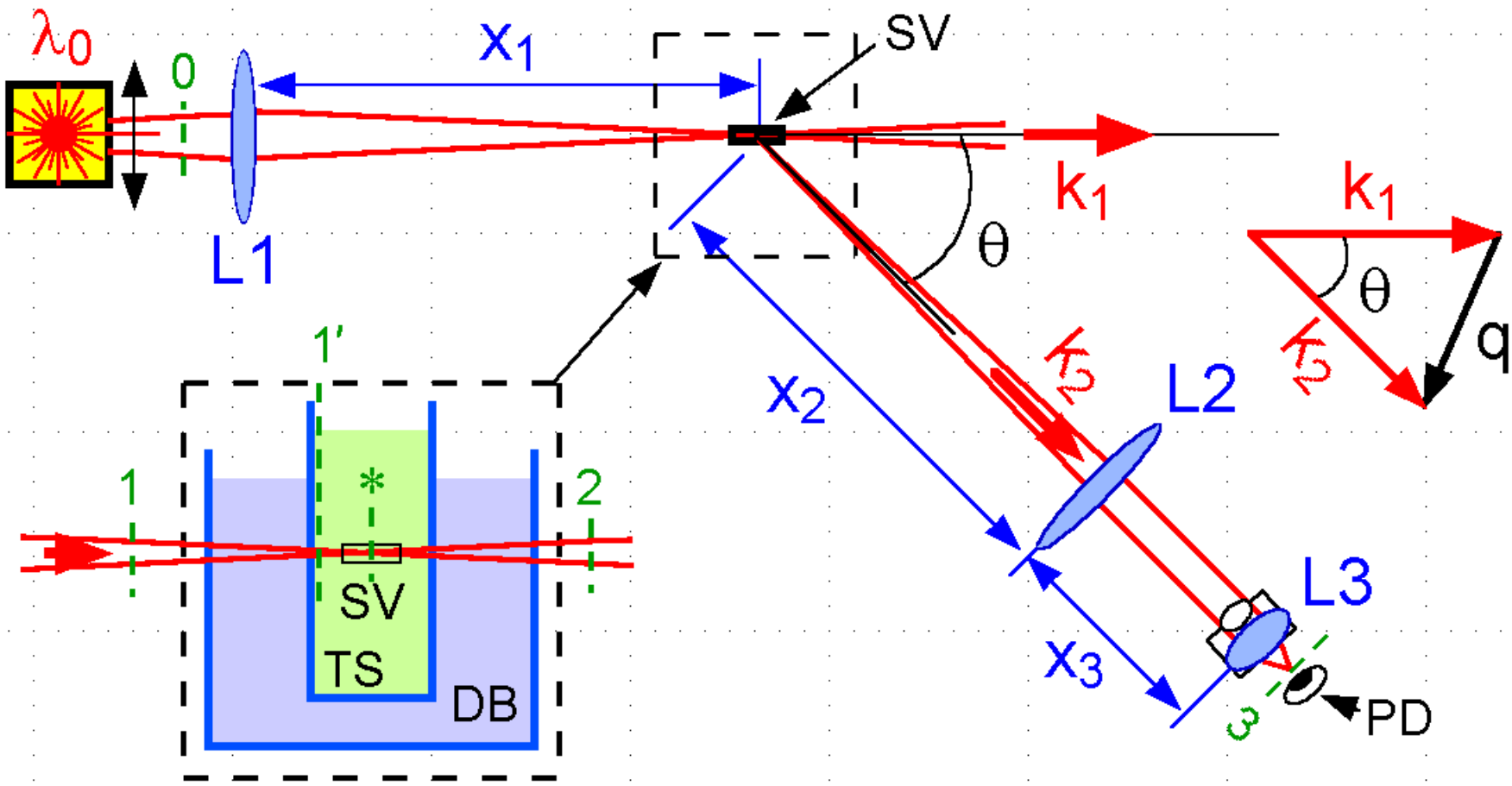

Fig. 2

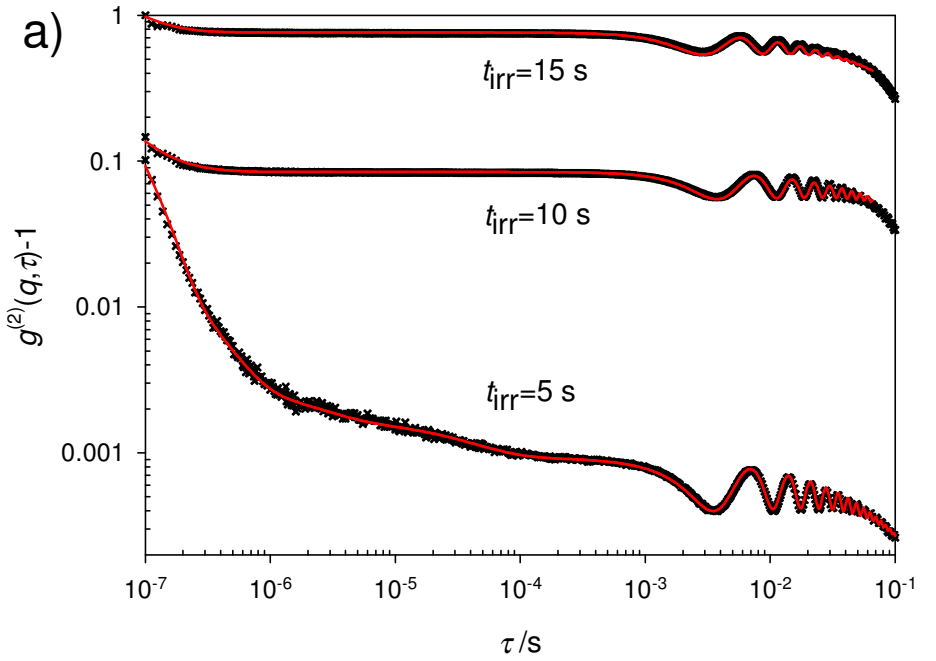
a)
1
0.1
0.01
0.001
$g^{(2)}(q,\tau)$-1
t_{irr}=15 s
t_{irr}=10 s
t_{irr}=5 s
10^{-7}
10^{-6}
10^{-5}
10^{-4}
10^{-3}
10^{-2}
10^{-1}
τ /s

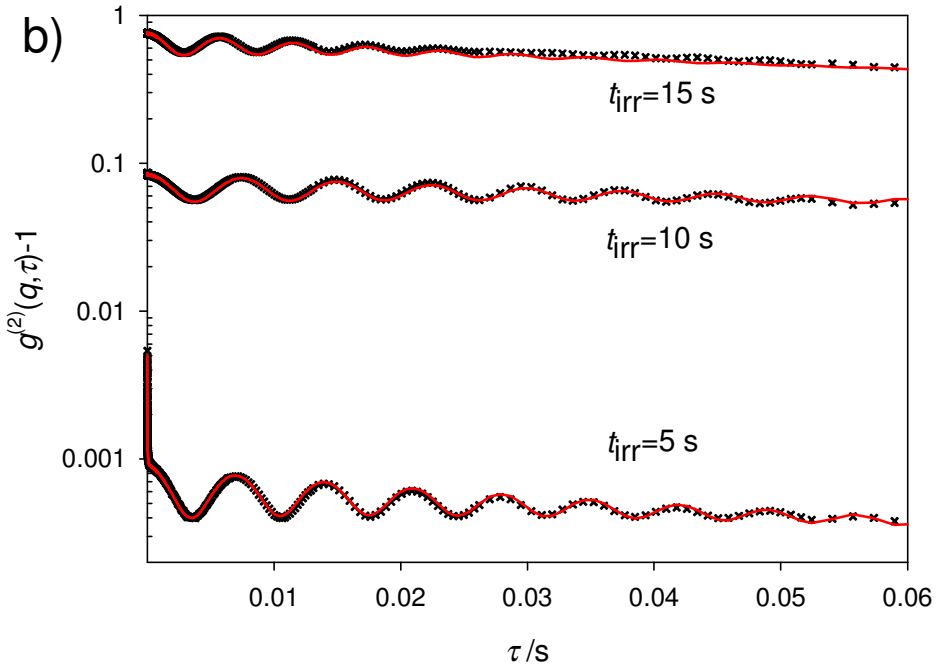
b)
1
0.1
0.01
0.001
$g^{(2)}(q,\tau)$-1
t_{irr}=15 s
t_{irr}=10 s
t_{irr}=5 s
0.01
0.02
0.03
0.04
0.05
0.06
τ /s

Fig. 3

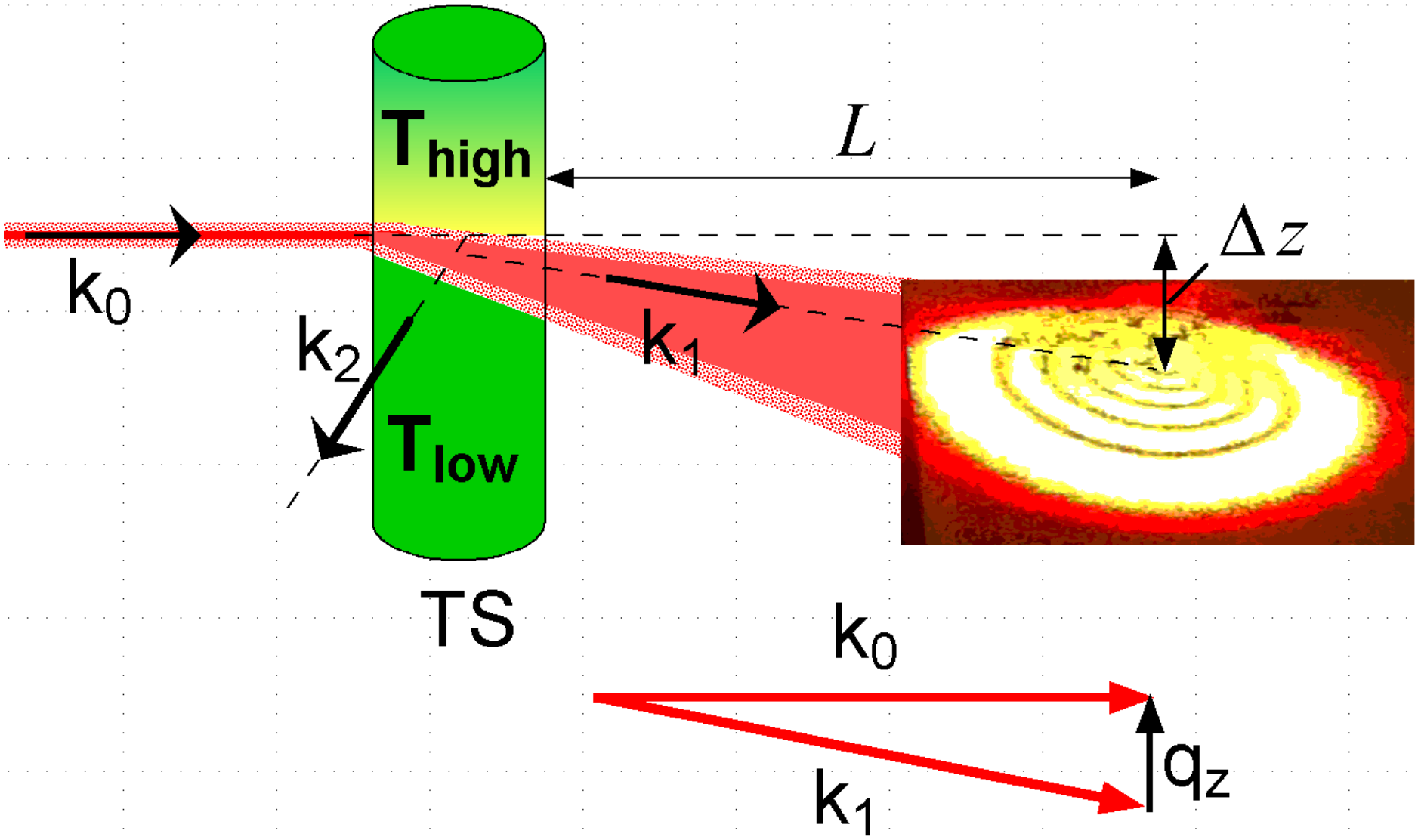

Fig. 4

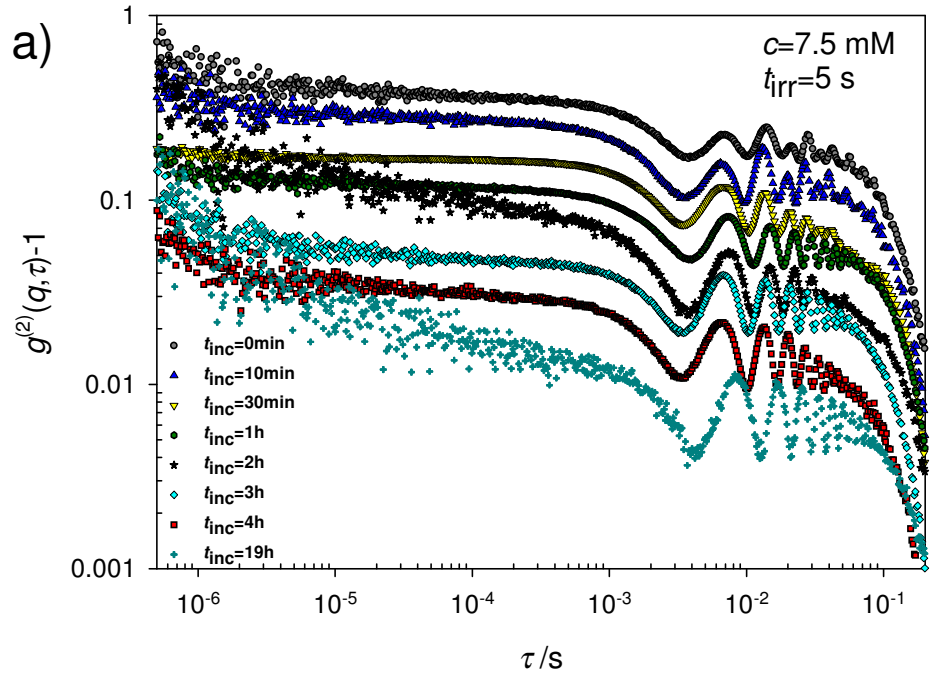
a)
c=7.5 mM
t_irr=5 s
g^(2)(q,τ)-1
τ /s
t_inc=0min
t_inc=10min
t_inc=30min
t_inc=1h
t_inc=2h
t_inc=3h
t_inc=4h
t_inc=19h

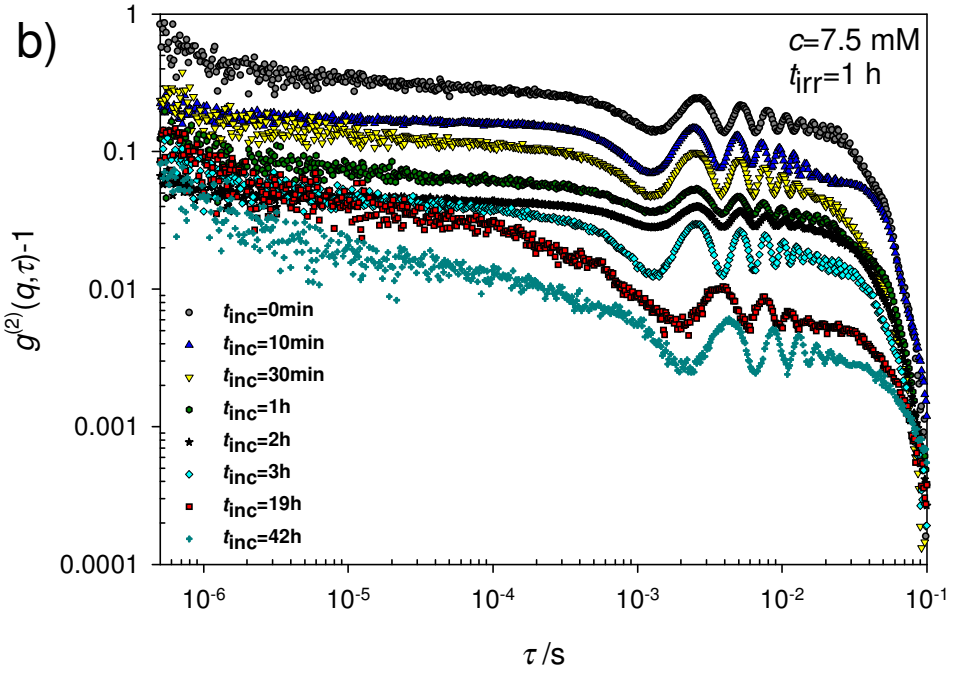
b)
c=7.5 mM
t_irr=1 h
g^(2)(q,τ)-1
τ /s
t_inc=0min
t_inc=10min
t_inc=30min
t_inc=1h
t_inc=2h
t_inc=3h
t_inc=19h
t_inc=42h

Fig. 5

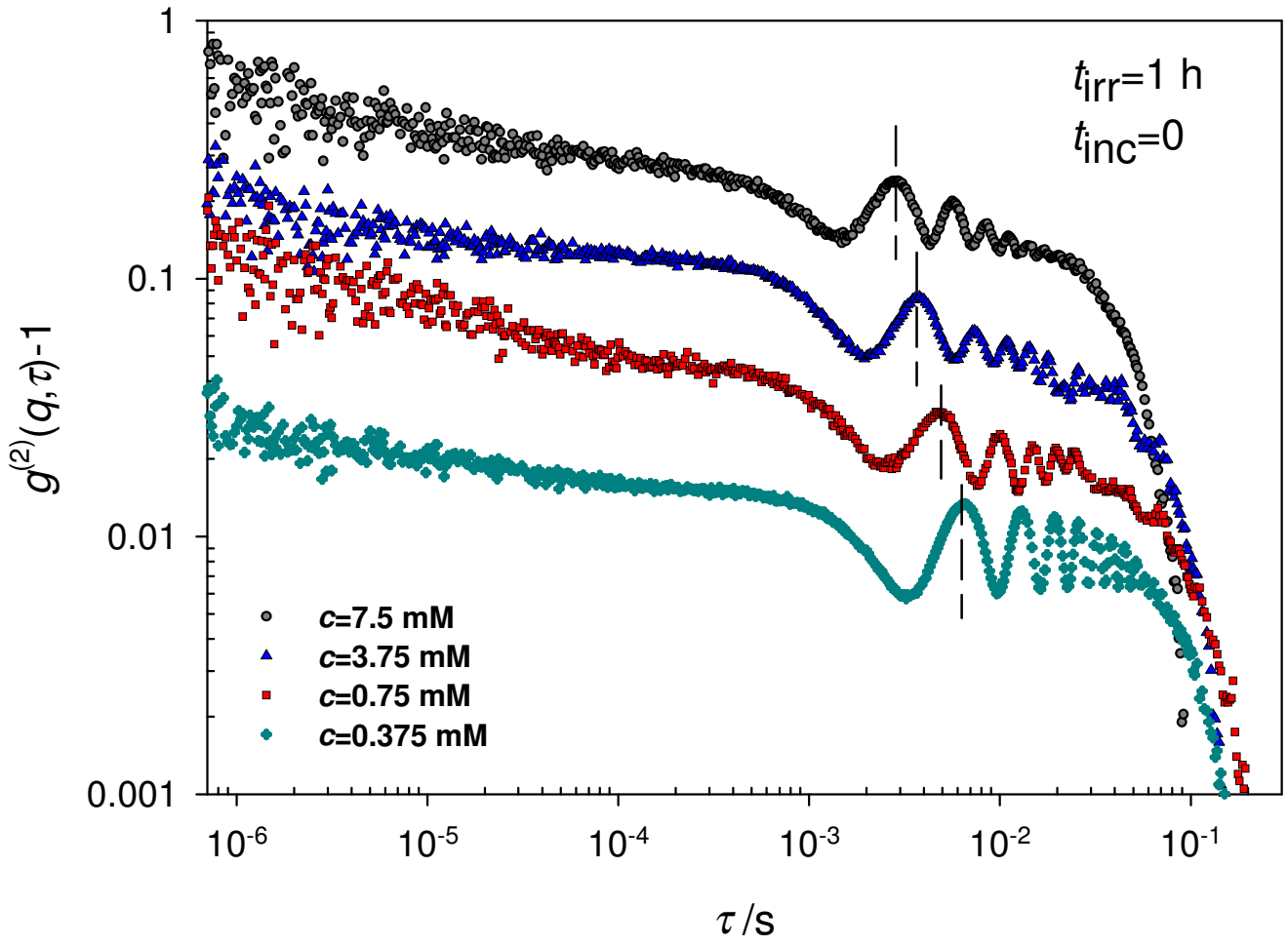
1
0.1
0.01
0.001
$g^{(2)}(q,\tau)$-1
t_{irr}=1 h
t_{inc}=0
c=7.5 mM
c=3.75 mM
c=0.75 mM
c=0.375 mM
10^{-6}
10^{-5}
10^{-4}
10^{-3}
10^{-2}
10^{-1}
τ /s

Fig. 6

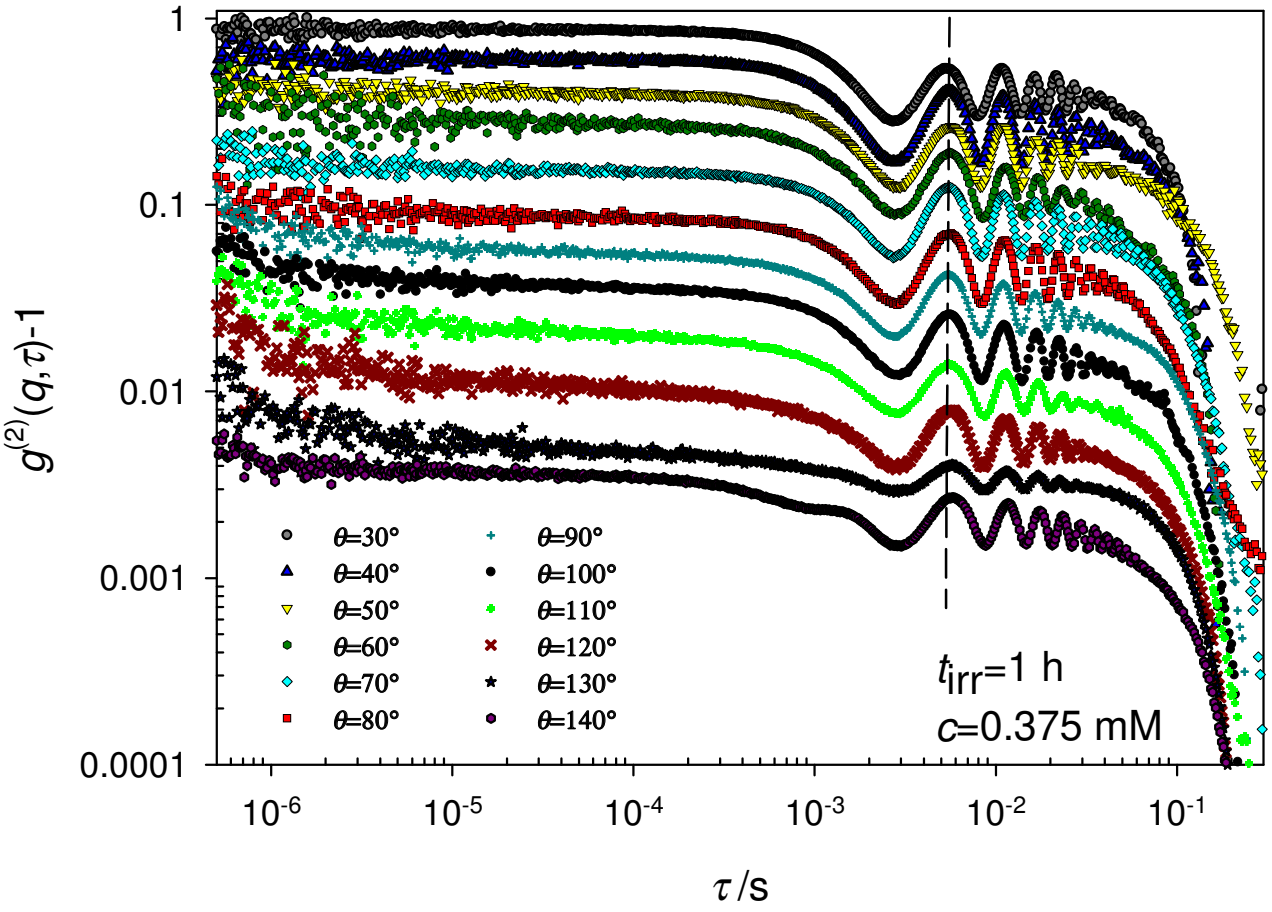
1
0.1
0.01
0.001
0.0001
$g^{(2)}(q,\tau)$-1
10^{-6}
10^{-5}
10^{-4}
10^{-3}
10^{-2}
10^{-1}
τ /s
θ=30°
θ=40°
θ=50°
θ=60°
θ=70°
θ=80°
θ=90°
θ=100°
θ=110°
θ=120°
θ=130°
θ=140°
t_{irr}=1 h
c=0.375 mM

Fig. 7

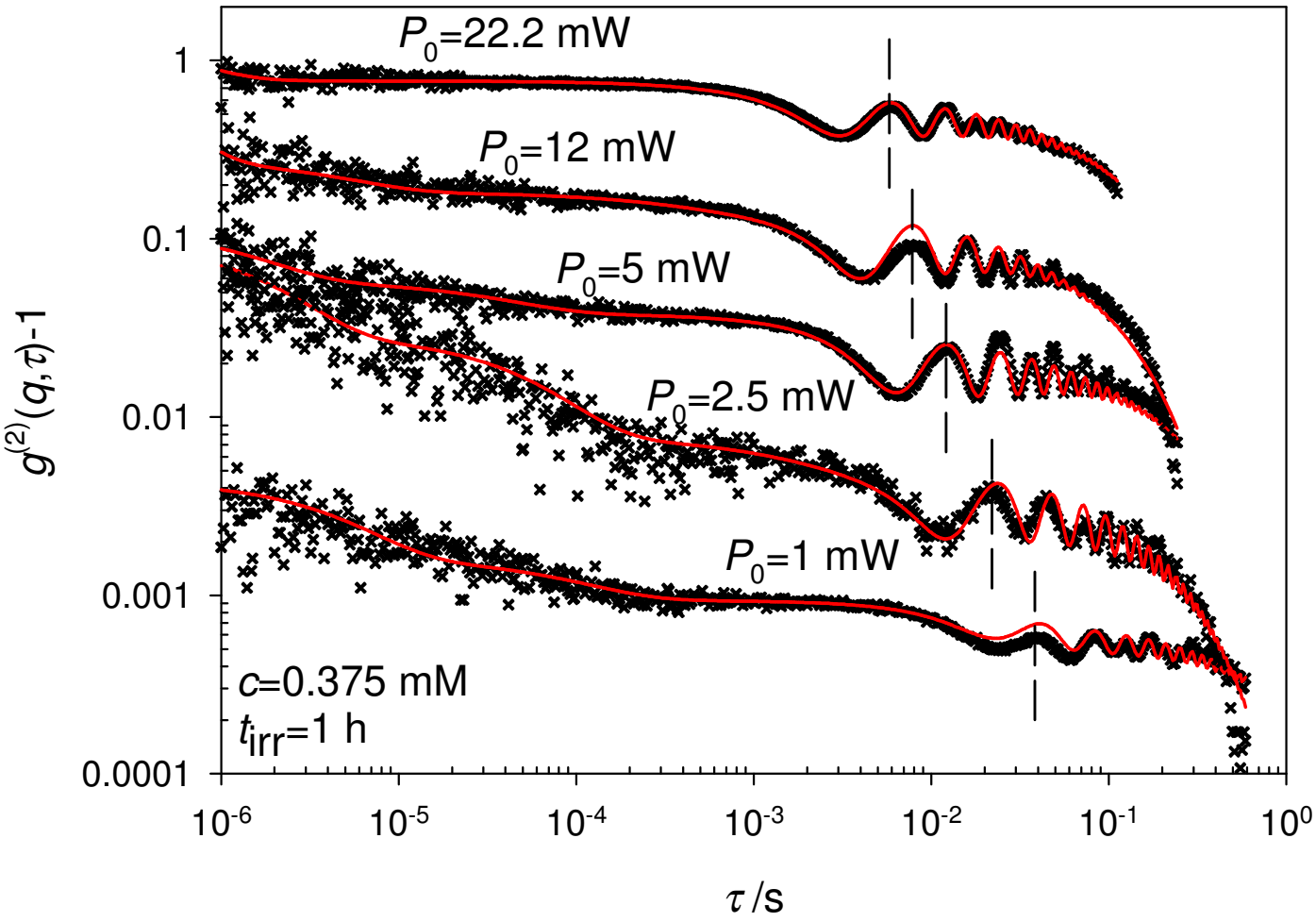
P_0=22.2 mW
P_0=12 mW
P_0=5 mW
P_0=2.5 mW
P_0=1 mW
c=0.375 mM
t_{irr}=1 h
$g^{(2)}(q,\tau)$-1
τ /s
1
0.1
0.01
0.001
0.0001
10^{-6}
10^{-5}
10^{-4}
10^{-3}
10^{-2}
10^{-1}
10^{0}

Fig. 8

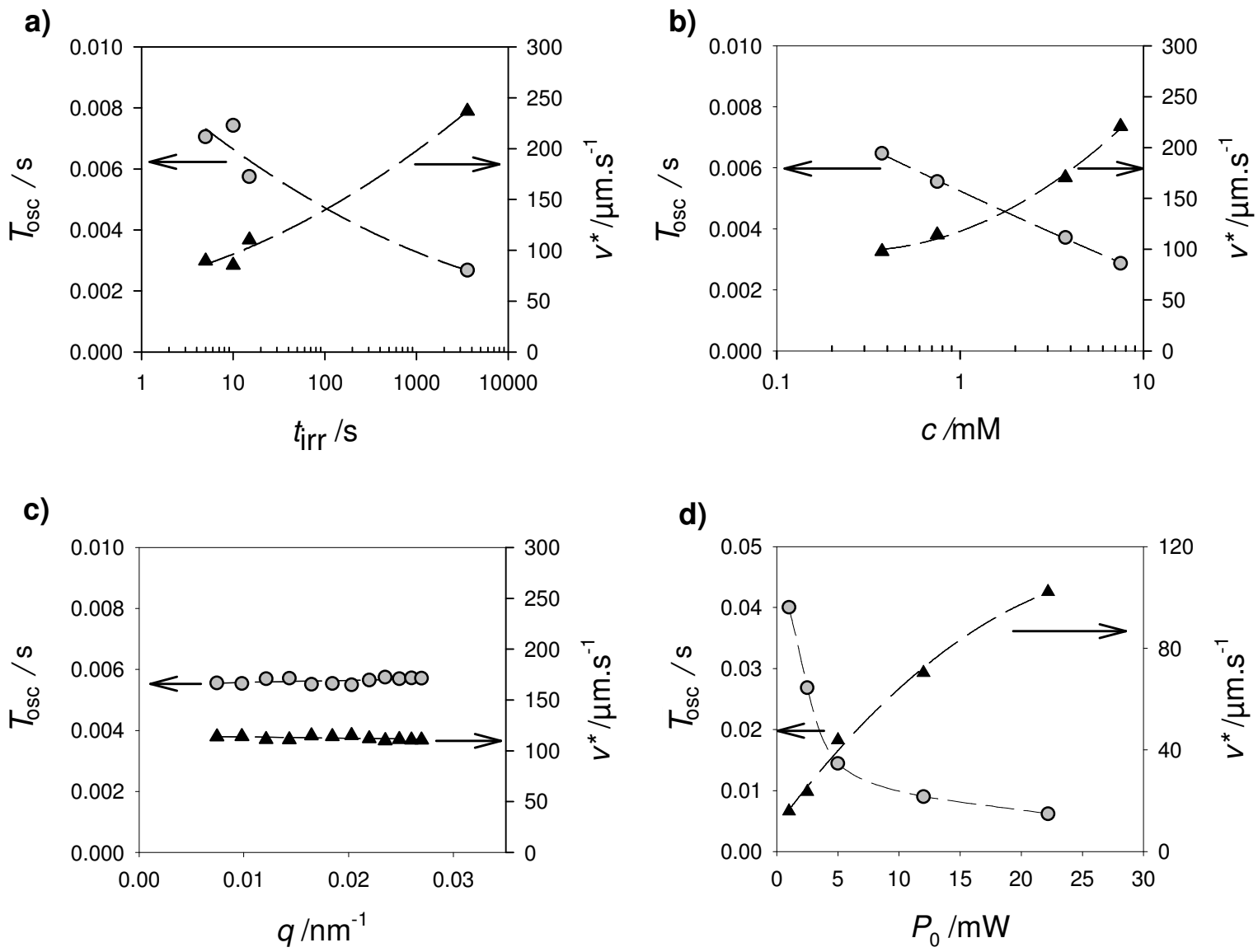

Fig. 9

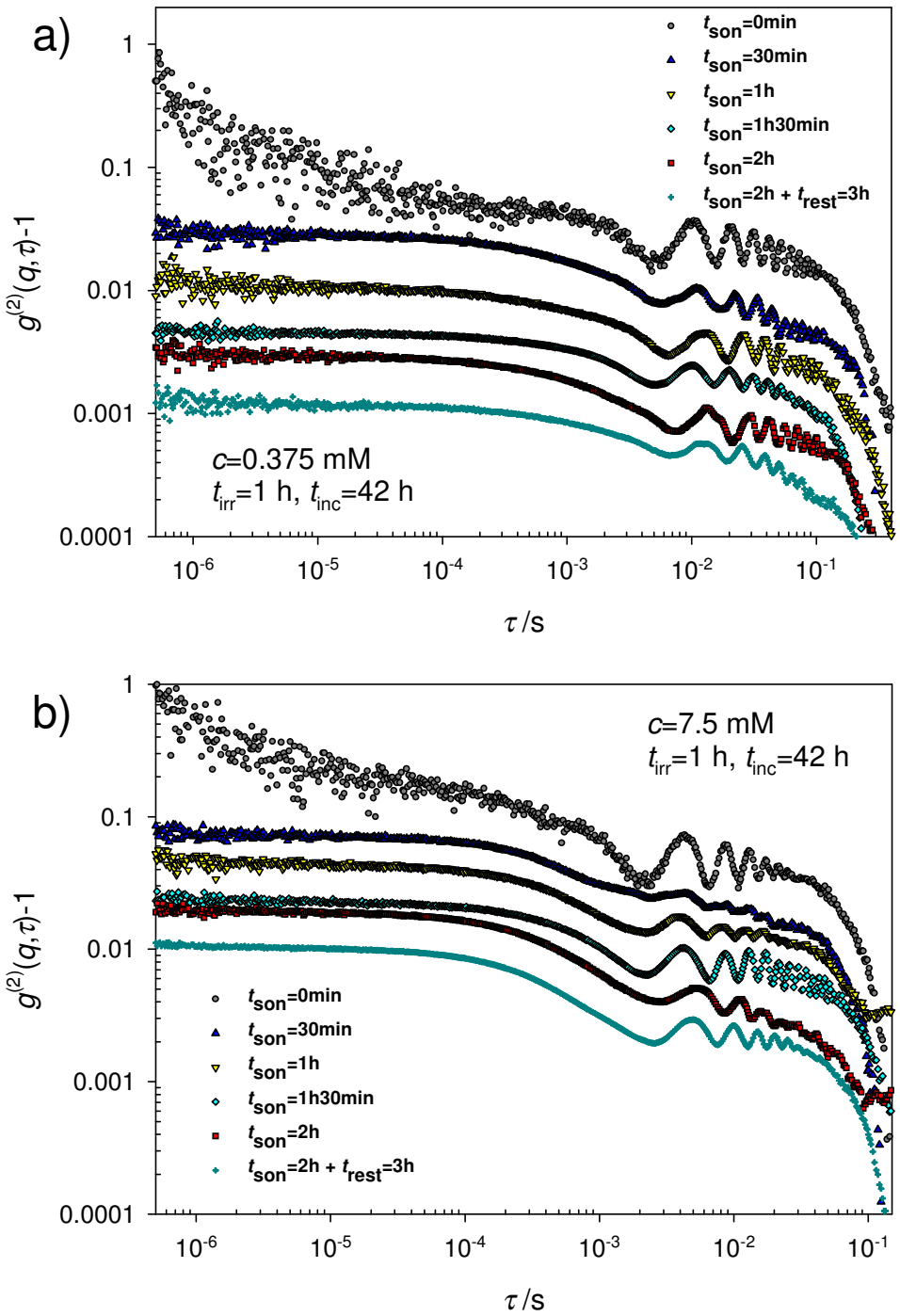
a)
t_{son}=0min
t_{son}=30min
t_{son}=1h
t_{son}=1h30min
t_{son}=2h
t_{son}=2h + t_{rest}=3h
c=0.375 mM
t_{irr}=1 h, t_{inc}=42 h
$g^{(2)}(q,\tau)$-1
τ /s
b)
c=7.5 mM
t_{irr}=1 h, t_{inc}=42 h
t_{son}=0min
t_{son}=30min
t_{son}=1h
t_{son}=1h30min
t_{son}=2h
t_{son}=2h + t_{rest}=3h
$g^{(2)}(q,\tau)$-1
τ /s

Fig. 10

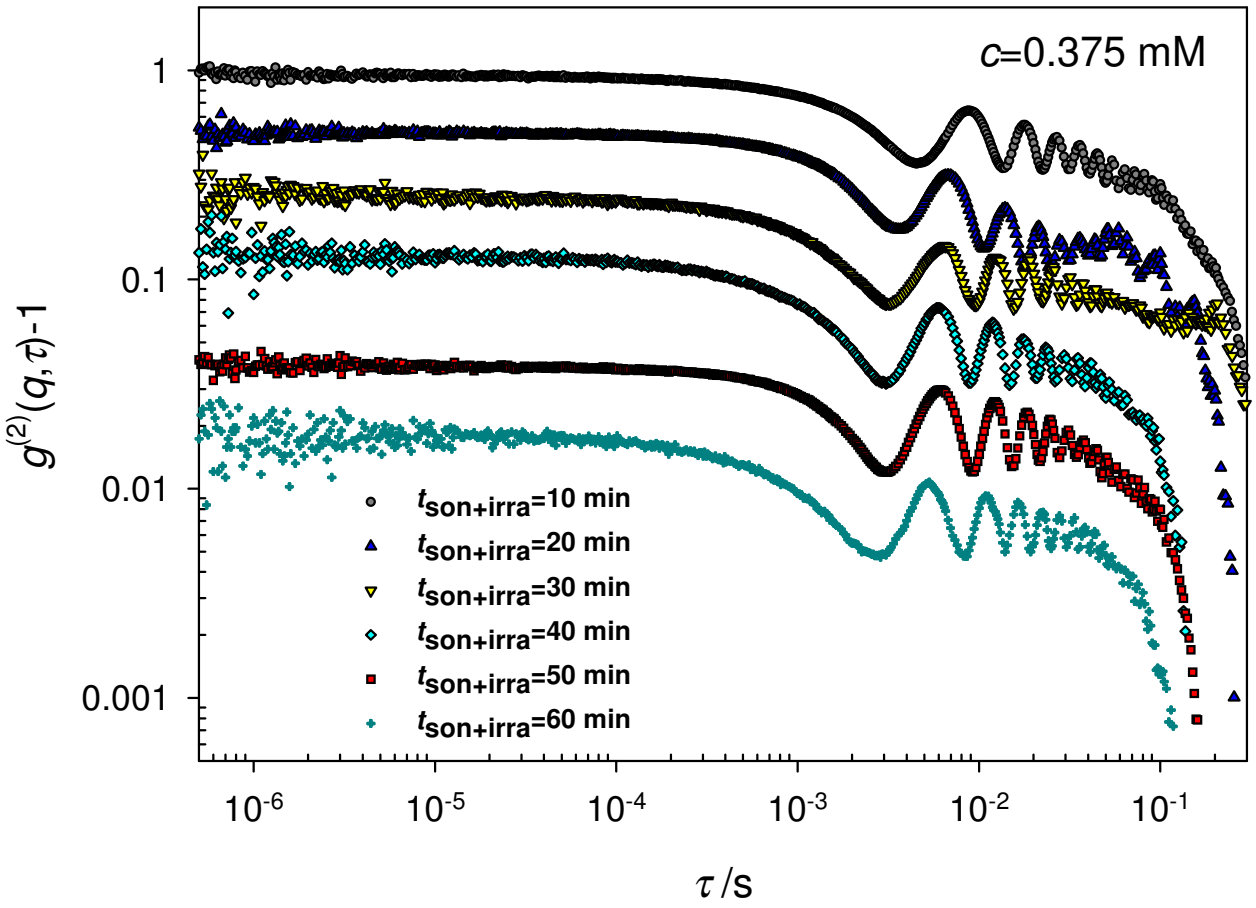
c=0.375 mM
1
0.1
0.01
0.001
$g^{(2)}(q,\tau)$-1
$t_{son+irra}$=10 min
$t_{son+irra}$=20 min
$t_{son+irra}$=30 min
$t_{son+irra}$=40 min
$t_{son+irra}$=50 min
$t_{son+irra}$=60 min
10^{-6}
10^{-5}
10^{-4}
10^{-3}
10^{-2}
10^{-1}
τ /s

Fig. 11

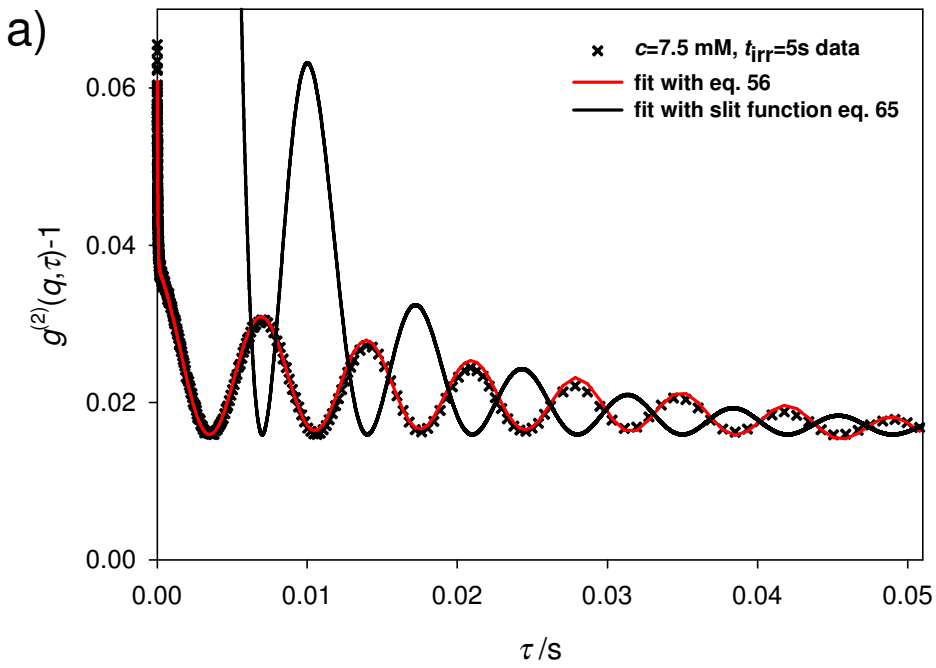
a)
c=7.5 mM, t_irr=5s data
fit with eq. 56
fit with slit function eq. 65
g(2)(q,τ)-1
0.00
0.02
0.04
0.06
0.00
0.01
0.02
0.03
0.04
0.05
τ /s

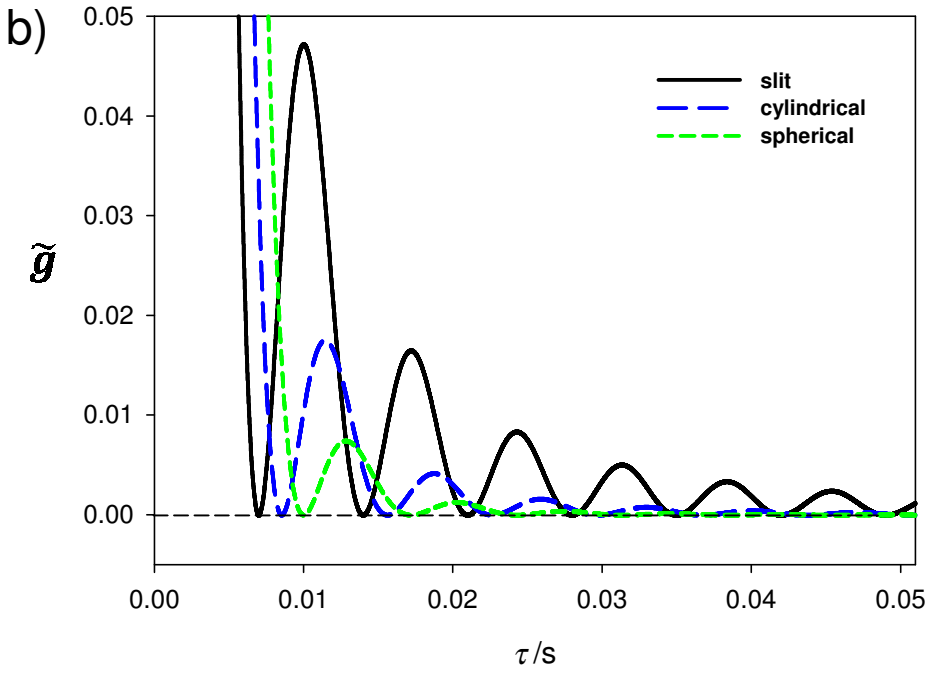
b)
slit
cylindrical
spherical
g̃
0.00
0.01
0.02
0.03
0.04
0.05
0.00
0.01
0.02
0.03
0.04
0.05
τ /s

Fig. 12

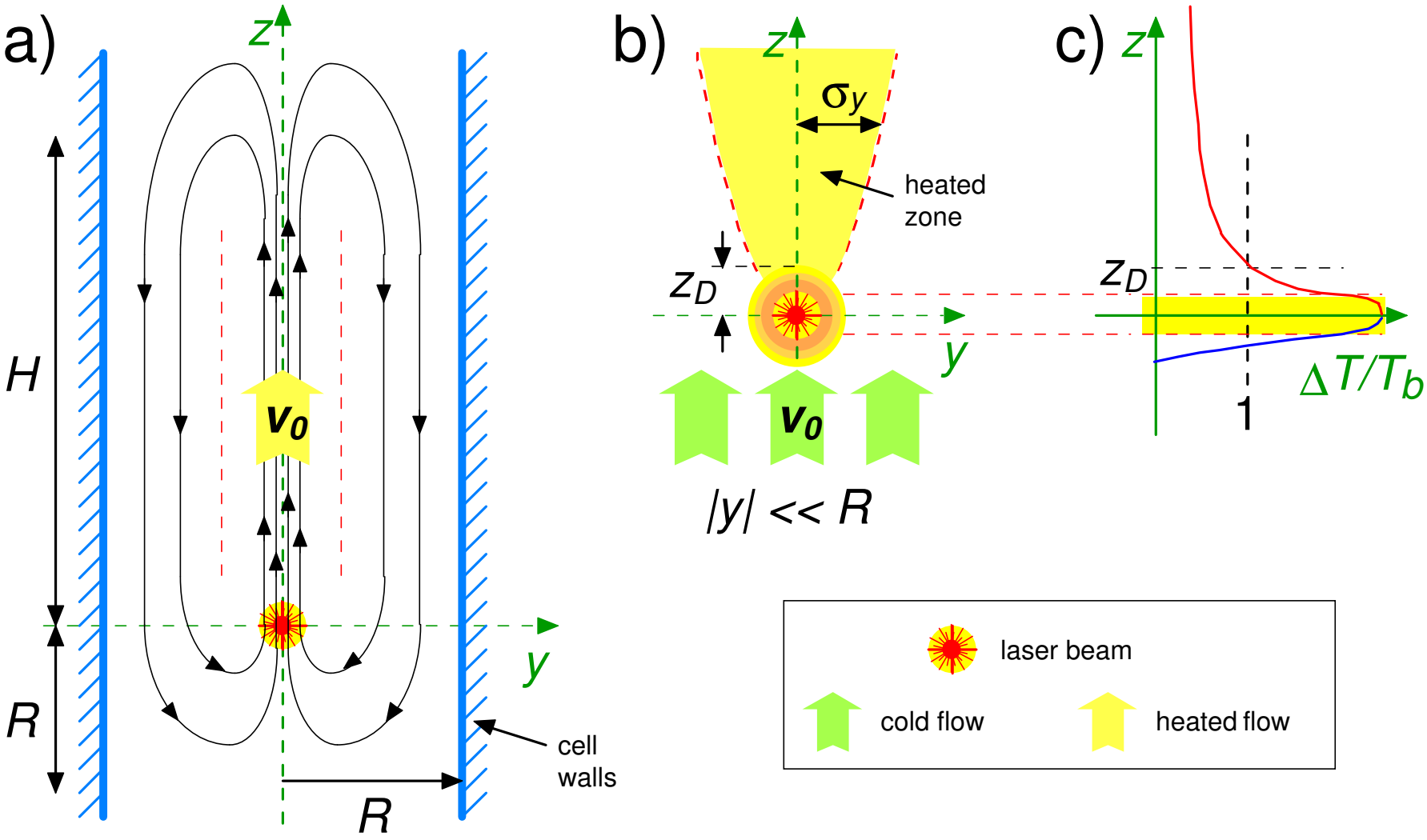
a)
z
H
v0
y
R
R
cell
walls
b)
z
σy
heated
zone
zD
y
v0
|y| << R
c)
z
zD
ΔT/Tb
1
laser beam
cold flow
heated flow

Fig. 13

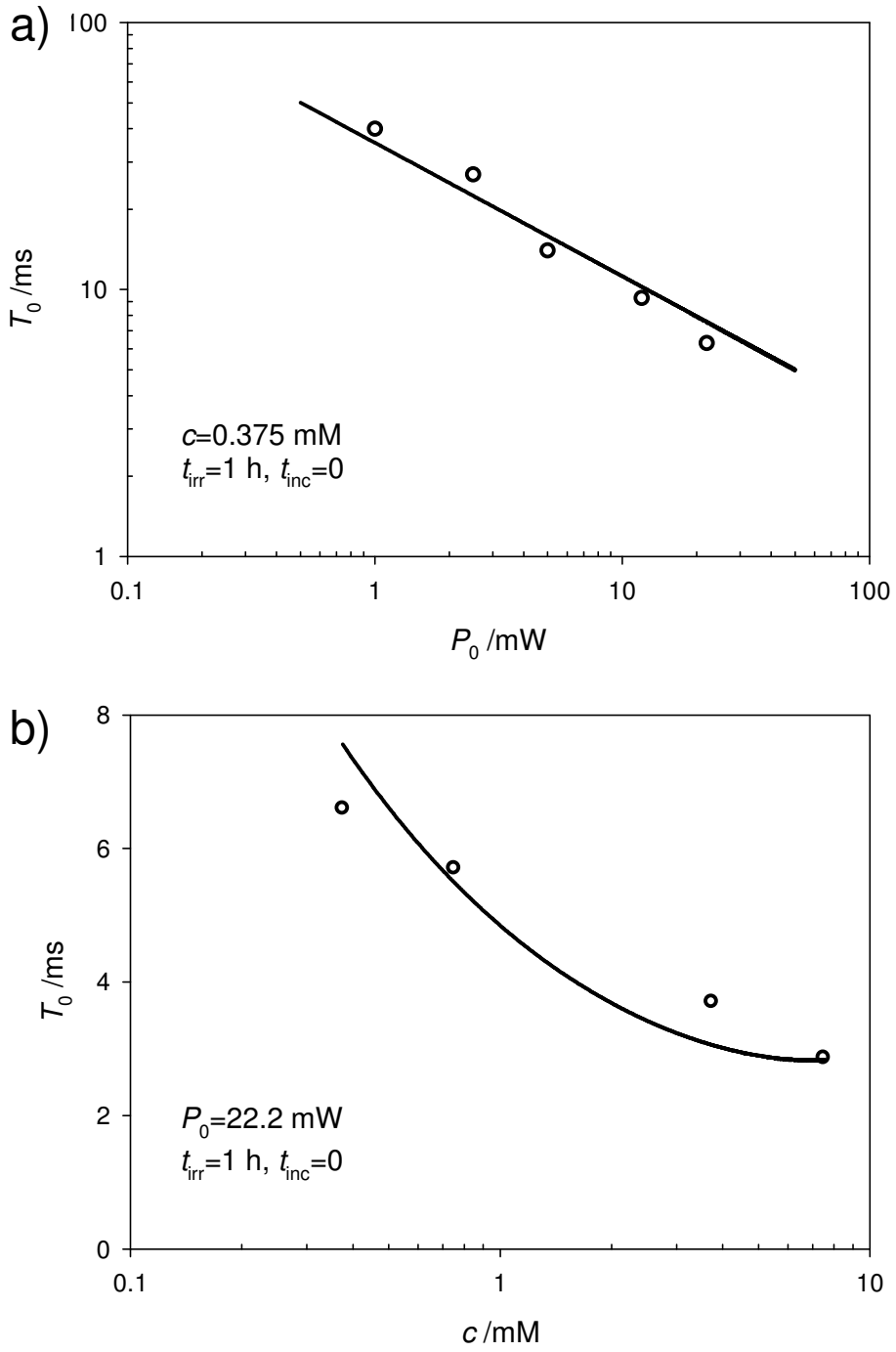
a)
100
10
1
T_0 /ms
c=0.375 mM
t_{irr}=1 h, t_{inc}=0
0.1
1
10
100
P_0 /mW
b)
8
6
4
2
0
T_0 /ms
P_0=22.2 mW
t_{irr}=1 h, t_{inc}=0
0.1
1
10
c /mM

Fig. 14

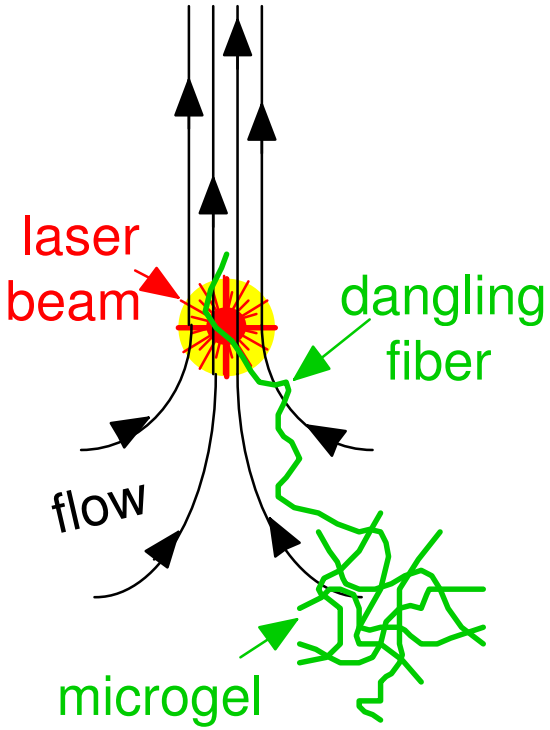

Fig. 15